

## **Response to Reviews – Esurf Manuscript**

### **The Effects of Late Cenozoic Climate Change on the Global Distribution of Frost Cracking**

By: Sharma et al.

#### **Response to Associate Editor: Michael Krautblatter**

Dear Prof. Krautblatter,

We would like to thank you for agreeing to be the associate editor of our manuscript. We also thank our two anonymous referees for their valuable comments and suggestions. We addressed each comment and suggestion by the reviewers and think it improved the quality of our manuscript and made it more useful to the prospective readers. We hope the revised manuscript also meets the referees' expectations and high standard of Esurf. The most important changes are summarized below

In response to RC1 regarding the unavailability of paleoclimate data to validate the model results (and regarding the scale issues), we revised our data comparison (Section 5.3) to emphasize on comparison of global (and general) trends of our FCI estimates with results from previous studies and provide suggestions for future regional studies (Section 5.5). We clarified the source of land surface paleo-temperature data and revised the methods section (Section 3.1) to explain and justify the use of sinusoidal daily temperatures. We revised the limitations section (Section 5.5) to highlight the problems of direct application of our model results in alpine studies due to coarse spatial resolution. We also clarified the source of glacier mask and modified our model results and Fig. 6-10 (and supplement Fig. 1-2), where FCI is masked with ice-sheet cover.

In response to RC2 we updated our model results and Fig. 6-10 (and supplement Fig. 1-2) to include 'maximum glacier mask during Pleistocene' in FCI estimates derived from the Pliocene simulations. We revised the model limitations (Section 5.5) to discuss uncertainties arising due to the coarse spatial resolution of soil data on modeled FCI. We also revised the discussion section (Section 5.1) to evaluate the influence of penalty function on FCI and elaborate on the importance of paleoclimate time-slices (for surface processes) based on globally summed FCI estimates.

We have provided the details of manuscript revision in the point-by-point response to the referees' comments. We deeply appreciate your and all referees' efforts to help us improve our manuscript.

The submission file consists of our cover letter, followed by point-by-point response to referees' comments, and the revised manuscript (with tracked-changes) specifying all the modifications made in accordance with the referees' comments.

Please contact us if further clarifications are required.

Sincerely,

Hemanti Sharma, Sebastian Mutz, and Todd Ehlers (corresponding author).

## Response to review AR1

The reviewer's comments are mentioned in black and author responses are in blue.

We thank the reviewer for her/his time and efforts in highlighting parts of the manuscript that require changes and clarification.

The paper "The Effects of Late Cenozoic Climate Change on the Global Distribution of Frost Cracking" by Sharma et al. presents the results of three frost cracking models applied on global scale. The authors used published temperature reconstruction in an 80 to 80 km resolution for four time slices: Pre-Industrial (~1850 CE, PI), Mid-Holocene (~6 ka, MH), Last Glacial Maximum (~21 ka, LGM) and Pliocene (~3 Ma, PLIO) times. These temperatures were used to calculate days spent in the frost cracking window (Anderson, 1998) and two existing frost cracking models (Andersen et al., 2015; Hales and Roering, 2007). The authors analyzed spatial variation of frost cracking intensity (FCI) at individual time slices and observed large deviations of FCI between warmer (PI) and colder (LGM) climate. The paper addresses an important topic about spatial and temporal variation of frost weathering that shapes the Earth's surface. My major concern is that there is no independent data set that enables the validation of the model results. The authors provide three model results but there is no possibility to review the model results for a location where data exist or for different time slices.

The reviewer raised a very important concern regarding the unavailability of data for paleoclimate time-slices to validate the model results. We addressed this in section 5.3 of the revised manuscript by comparing the trends of our global FCI estimates with results from previous studies. Due to the scarcity of regional data, we focus on the global and general trends in these comparisons and provide a few suggestions (e.g. in section 5.5) for future regional studies that will result in a better basis for detailed regional estimates and their validation.

Lastly, we briefly mention here a, perhaps, philosophical difference with the reviewer in how models should be used. Throughout geoscience literature, numerical models play a role in the formulation of hypotheses that can be tested in observational studies. Models are useful for hypothesis formulation because the underlying physics/processes producing different observables are known/controlled for. Observations, in contrast, are useful for telling us what has happened, but they often (not always) do not tell you the process(es) responsible for the observations recorded. There is no shortage of observational studies that lack a process based (modeling) framework to be interpreted, and instead infer (qualitatively) the underlying process. The two approaches (models, observations) go hand in hand and science progresses by development in both approaches. This was our motivation for conducting a global scale modeling analysis of frost cracking (and for setting up the simulations in Mutz et al., 2018; and Mutz and Ehlers, 2019, ESurf).

Concerning paleoclimate model validation – the standard approach used in this community is to conduct present-day simulations that are compared to observations (usually reanalysis data). Our previous published work does this with the ECHAM5 model (for the same time slices presented in this study). If the comparison is satisfactory, then the modeling approach that follows is to modify boundary conditions and model inputs (e.g., land cover, sea surface temperatures, etc.) for paleo conditions. Our experience in our previous publications is that the differences between a climate model results and reanalysis data (e.g., ERA40) for a region is typically less than the differences between different reanalysis data sets. This has repeatedly been shown for the ECHAM5 model (it has been around a while). In short, observed climate is not as well resolved as many people think, and model performance (at for ECHAM5 at least) is reliable for (paleo)climate studies. The assumption then made is that if the physics in the model worked correctly for the present-day, then they also work for the paleoconditions and meaningful comparisons to the modern can be made by differencing modern and paleo simulation results. This is the underlying approach of this community, and also what we follow in this manuscript.

Concerning frost cracking observations available to test model predictions: Later in this review we address the reviewers concern regarding which observational studies provide a meaningful comparison to the model results. We now focus our comparison to regional observations/studies only.

## **1. The use of paleodata**

The study uses paleo-temperatures, which are air temperatures according to the papers by Mutz & Ehlers (2019) and Mutz et al. (2018) and not land surface temperatures as indicated in this paper. Snow cover and vegetation will result in temperature offsets between air and surface temperatures, which will cause large difference in the frost cracking results and are not addresses in this manuscript at all.

The reviewer raises a good point here, however her/his statement is due to our lack of clarity in the text (which we've now fixed). Our analysis was actually conducted on the ground temperatures. The above-mentioned studies i.e., Mutz & Ehlers (2019) and Mutz et al. (2018) used 2m air temperature in their analyses (as the reviewer states). However, the palaeoclimate experiments are conducted with a GCM (ECHAM5-wiso) that simulates more aspects and variables of the climate system. Snow and vegetation cover are included in the GCM's simulation of an equilibrium climate, and (land) surface temperature are computed and saved in the GCM's standard output along with various other variables. These have been available for download since their first publication in 2018 along with 14 other variables because they were not analyzed those studies. Not all were presented in the papers, but some have already

been used in other studies (e.g. Werner et al. 2018, ESurfD). These can be downloaded as part of the p001 package from:

<https://esdynamics.geo.uni-tuebingen.de/wiki/index.php/all-category/2-main/117-echam5-palaeoclimate-simulations-mutz-et-al-2018>

Hence, we confirm that we did in fact use land surface temperature data in the study and obtained them from the Mutz et. al. (2018) simulations. We have mentioned this contribution in Acknowledgements section (lines 592-593). We have also added this point in the revised manuscript in Data section (line 83-85).

The paleo-data is available at 80 to 80 km resolution which is much too coarse to apply these to high-topographic environments as the European Alps, Andes or Tibetan Plateau. The coarse resolution is not integrating topographic effects in is not applicable to mountains. The authors should downscale their data, which is a standard procedure in alpine studies (e.g. Fiddes and Gruber, 2014).

As a bit of background: Typically when we publish our climate model results the climate community modelers/reviewers complain that our resolution for the simulations is excessively high (not too low)!. The reasons for them saying this is that lower resolution simulations run significantly faster and capture them sample climatology as the higher resolution models. We have been insistent to the climate modeling community in running our simulations at a high resolution (80x80km) globally because they are more useful for comparison to geomorphic studies (such as this manuscript). Thus, by climate community standards, - the simulations presented in this study are very high resolution. They also took about 2 months each to run on a large cluster, running them at an even higher resolution (e.g., T256) would likely take 9-12 months (each).

In this study, we attempt to present a first order (global) approximation of frost cracking intensity subjected to different Cenozoic time-slices. We state this clearly in the text, and our interpretations (e.g., all the figures) are conducted at regional and global scales only. Dynamical downscaling of a palaeoclimate simulation (e.g. Wang et al. 2021, JGR-Atmospheres) would be ideal in such a case and preferable over simple topographic corrections that do not adequately consider the impact of topography-related atmospheric dynamics leading to further changes in climate elements (incl. surface temperature). However, this is only feasible for studies focusing on one region, as regional climate simulations for only one orogen would likely take several months to a year, depending on the researcher's level of expertise and challenges encountered along the way. The application of such regional climate models (or even simpler downscaling approaches suggested by the reviewer) would require

additional expertise/training and significant computation time that is beyond the scope of this study. Furthermore, Pliocene downscaling is complicated further by uncertainties in topographic reconstruction on a much finer scale. We therefore decided to not pursue the idea of global-scale climate downscaling in orogens and instead clarify our focus on global first order trends in the introduction section 1 (lines 68-69). Additionally, we make recommendations for future regional/local studies (e.g., in high-topographic environments) that warrant the intermediate step of climate downscaling (lines 528-533 in the limitation section 5.5), but please note that each of these studies would likely be a paper/study in itself and could not present a global analysis as we've done here.

The data is available at daily time steps and could be used directly to calculate frost cracking. However, the authors calculate a mean annual temperature and half amplitude of annual temperature. They used sinusoidal daily temperatures but it remains unclear if these temperatures are from the paleo-temperatures or assumed values. A more direct use of paleo-temperatures would be better suited.

We prefer using sinusoidal daily temperatures over paleo-temperatures at daily time-steps for following reasons: Daily temperature variations predicted by GCMs are difficult to validate. Consequently, we do not expect any added value to forcing the frost-cracking models with GCM temperatures instead. Also, using daily temperatures instead of sinusoidal variations based on MAT and Ta would require relatively longer computation time for a global analysis like ours. Using the GCM temperature cycle is thus unlikely to produce significantly different results and we opt for the computationally more efficient option. However, we agree that in future local studies, using paleoclimate data at daily time-steps could provide higher accuracy to the model results with respect to time and depth of occurrence of frost cracking if daily variations are demonstrated to reflect realistic conditions in the study area at a specific time in the past. To our knowledge, the latter has not been demonstrated for the regions and time slices treated here. We have added the main reasons for our choice in the methods section 3.1 (lines 148-151).

## **2. Frost cracking models**

The authors used three proxies or models for frost cracking but only focus on model 3 in their paper. The days spent in the frost cracking window is only a poor proxy for frost cracking (Anderson et al., 2013). The model by Hales and Roering (2007) is out-dated and not including any lithological differences. Both models are barely used in the results and discussion section, therefore they could be omitted from the manuscript.

The first two proxies for frost cracking used in our study are simpler models, which require fewer input parameters and may still be used when a first order approximation is needed, especially when all required inputs for a more complex model are not available. Hence, we include the results of simpler models i.e., model 1 (Anderson et al., 1998) and model 2 (Hales and Roering, 2007), in the main text, but still include them entirely in the supplement for reference. These results are still of potential use to the broader community and have merit when insufficient data is available to constrain a more complex model.

Finally, the second reviewer of this manuscript appreciated having all three models and requested a more detailed comparison between them (which we've done – see response to reviewer AR2).

The model by Andersen et al. (2015) is applied using soil thickness to constrain a soil layer with an assumed porosity of 30% which is located above a bedrock layer of 2% porosity. The soil thickness is derived from a global database with 5 km resolution and used for every time slice, however, it is unrealistic that soil thickness is a constant over Cenozoic time scales.

We agree that it is an unrealistic assumption to have a constant soil thickness over Cenozoic time-scales. However, there is no available dataset for past soil thickness, so we have used the present-day data, and clearly stated that it is a limitation. To address this concern, we have added additional text (lines 87-93) in the Data description (section. 2) and revisit it again in the model limitations section (section. 5.5, lines 508-514), to explain this limitation more prominently. We have also changed the caption of Fig. 1 to support our argument for the above assumption.

The substrate classification into soil and bedrock changes water flow in the subsurface within the frost cracking model. For alpine regions the database provides relative high soil depths, however, rockwalls with 30 % porosity are not existing, which highlights the problem of spatial solution and applicability of this model in this way to alpine conditions using a soil map. In addition, the model by Andersen et al. (2015) uses a fixed frost cracking widow between -8 and -3 °C that is not supported by laboratory data (e.g. Murton et al., 2006), field data (Girard et al., 2013) or physical models (Walder and Hallet, 1985). As lithology and rock strength show variations across the Earth, lithology will control weathering, which could be incorporated to include more realistic results.

We agree that the models are based on simplistic assumptions with coarse spatial resolution in paleoclimate and soil data. The model results cannot replace in-depth regional studies using high spatial resolution lithological distribution and downscaled (topographically corrected) paleoclimate data. We thank you for raising a very important concern. We have modified the

model limitations section 3.5 (lines 526-531) to include highlight these simplifications and avoid overinterpretation of our results.

We would like to thank the reviewer for raising the concern about the assumption of fixed frost cracking window. We have added the above argument in Introduction section 1 (lines 55-60) in the revised manuscript.

### **3. Glaciation**

The authors provide a glacier mask in the supplementary and compare this mask to FCI. The glacier mask is not including any glaciations in the European Alps during LGM or 1850 (Little Ice Age). On which scientific basis is the map derived? Why are the authors comparing the spatial distribution of FCI with their glacier mask? When a glacier is there, then there is no frost cracking as the rock is disconnected to atmospheric processes (Grämiger et al., 2018). By not including a glacial cover, the authors are overestimating the FCI by far.

The paleoclimate time-slice specific glacier masks (ice cover reconstructions) are the same as those that serve as input for the Mutz et al. (2018) simulations. In turn, Mutz et al. (2018) follow the experiment protocols of the Paleoclimate Modelling Intercomparison Project (PMIP) (Bracannot et al. 2012), also described on the PMIP3 wiki ([wiki.lscce.ipsl.fr/pmip3/doku.php/pmip3:index](http://wiki.lscce.ipsl.fr/pmip3/doku.php/pmip3:index)). This mask describes a synthesis of significant ice sheet cover, but does not account for different reconstructions or all regions covered by glaciers at the time. While PMIP4 has moved to the use of several different ice sheet and mask reconstructions for the LGM (Kageyama et al., 2021), PMIP3 use one reconstruction that comprises a synthesis of several reconstructions of significant ice cover (that would significantly impact climate). This is described in detail in Abe-Ouchi et al. (2015), which we list as the source for our boundary conditions in Table. 1 in the manuscript. We have also mentioned the source of glacier masks in the captions of Fig. 6-10 in revised manuscript.

Furthermore, in the revised manuscript, the glaciated regions in different time-slices were masked from the FCI results in different time-slices in all the three models. Also, in Pliocene simulations, regions which experienced glaciation during the Pleistocene, have been removed from the results. We do this, as the assumption of constant soil cover is heavily violated in regions that experienced Pleistocene glaciation (as mentioned in RC2.1). The glacier covers for respective Cenozoic time-slices have been masked and highlighted with distinct color (violet) in Fig. 6-10 and supplement Fig. 1-2.

Note that we were comparing the FCI difference maps to the glacier mask, as a comparison of FCI inside and outside the ice sheets in different time-slices creates confusion. This has

been rectified in the revised manuscript, where we have applied the glacier mask to the FCI difference maps too (Fig. 8-10). Hence, we do not compare glacier mask and FCI difference maps in the revised manuscript. Hopefully these modifications and explanations meet with the reviewer's approval.

#### **4. Scale issues**

The authors use a simple bottom-up approach to model frost cracking for different time slices. They have no independent data that they could use to validate their models. Consequently, they have a problem to discuss their own results and put them into a perspective. They compare a 80 x 80 km model for North America and Alaska for PI, MG and PLIO to a frost cracking studies at Jungfraujoch that measured frost weathering using acoustic emissions on one rockwall at 3500 m for 4 days (Amitrano et al., 2012) or one year (Girard et al., 2013). I cannot see how these studies support the author's results on much larger scale at different time steps in the past in completely different environments. Furthermore, the author states that their model results at higher Asia and Alaska during LGM are consistent to periglacial processes observed in Oregon (Marshall et al., 2015; Marshall et al., 2017). I cannot see the context between periglacial conditions and landforms in Oregon and the author's observed FCI in other areas of the Earth. These are just a few examples but the whole discussion shows no argumentation. Model results will be compared to models from Hales and Roering (2007) or Andersen et al. (2015), which are used to derive the same model results.

The reviewer makes a very valid point regarding scale differences. We have revised the data comparison section 5.3 to exclude the short-term studies and focus the revised section on discussion of broader trends and their comparison to more comparable findings by previous studies. Additionally, we highlight the need for scale-bridging for regional studies (lines 531-533 in the limitation section).

#### **References cited in our response:**

Anderson, R. S.: Near-surface Thermal Profiles in Alpine Bedrock: Implications for the Frost Weathering of Rock, *Arctic and Alpine Research*, 30, 362–372, <https://doi.org/10.1080/00040851.1998.12002911>, 1998.

Abe-Ouchi, A., Saito, F., Kageyama, M., Braconnot, P., Harrison, S. P., Lambeck, K., Otto-Bliesner, B. L., Peltier, W. R., Tarasov, L., Peterschmitt, J.-Y., and Takahashi, K.: Ice-sheet configuration in the CMIP5/PMIP3 Last Glacial Maximum experiments, *Geosci. Model Dev.*, 8, 3621–3637, <https://doi.org/10.5194/gmd-8-3621-2015>, 2015.



Braconnot et al, Evaluation of climate models using palaeoclimatic data, *Nature Climate Change* 2, 417-424 (2012), doi:10.1038/nclimate1456

Hales, T. C. and Roering, J. J.: Climatic controls on frost cracking and implications for the evolution of bedrock landscapes, *J. Geophys. Res.*, 112, F02033, <https://doi.org/10.1029/2006JF000616>, 2007.

Kageyama, M., Harrison, S. P., Kapsch, M.-L., Lofverstrom, M., Lora, J. M., Mikolajewicz, U., Sherriff-Tadano, S., Vadsaria, T., Abe-Ouchi, A., Bouttes, N., Chandan, D., Gregoire, L. J., Ivanovic, R. F., Izumi, K., LeGrande, A. N., Lhardy, F., Lohmann, G., Morozova, P. A., Ohgaito, R., Paul, A., Peltier, W. R., Poulsen, C. J., Quiquet, A., Roche, D. M., Shi, X., Tierney, J. E., Valdes, P. J., Volodin, E., and Zhu, J.: The PMIP4 Last Glacial Maximum experiments: preliminary results and comparison with the PMIP3 simulations, *Clim. Past*, 17, 1065–1089, <https://doi.org/10.5194/cp-17-1065-2021>, 2021.

Mutz, S. G. and Ehlers, T. A.: Detection and explanation of spatiotemporal patterns in Late Cenozoic palaeoclimate change relevant to Earth surface processes, *Earth Surf. Dynam.*, 7, 663–679, <https://doi.org/10.5194/esurf-7-663-2019>, 2019.

Mutz, S. G., Ehlers, T. A., Werner, M., Lohmann, G., Stepanek, C., and Li, J.: Estimates of late Cenozoic climate change relevant to Earth surface processes in tectonically active orogens, *Earth Surf. Dynam.*, 6, 271–301, <https://doi.org/10.5194/esurf-6-271-2018>, 2018.

Taylor, K.E., R.J. Stouffer, G.A. Meehl: An Overview of CMIP5 and the experiment design.” *Bull. Amer. Meteor. Soc.*, 93, 485-498, doi:10.1175/BAMS-D-11-00094.1, 2012.

Wang, X., Schmidt, B., Otto, M., Ehlers, T. A., Mutz, S. G., Botsyun, S., and Scherer, D. Sensitivity of water balance in the Qaidam Basin to the mid-Pliocene climate. *Journal of Geophysical Research: Atmospheres*, 126, e2020JD033965. <https://doi.org/10.1029/2020JD033965>, 2021

Werner, C., Schmid, M., Ehlers, T. A., Fuentes-Espoz, J. P., Steinkamp, J., Forrest, M., Liakka, J., Maldonado, A., and Hickler, T.: Effect of changing vegetation and precipitation on denudation – Part 1: Predicted vegetation composition and cover over the last 21 thousand years along the Coastal Cordillera of Chile, *Earth Surf. Dynam.*, 6, 829–858, <https://doi.org/10.5194/esurf-6-829-2018>, 2018.

## Response to review AR2

The reviewer's comments are mentioned in black and author responses are in blue.

We thank the reviewer for her/his time and efforts in highlighting parts of the manuscript that require changes and clarification.

1. The assumption of soil cover being comparable in the Pliocene is likely most heavily violated in regions that experienced Pleistocene glaciation. I suggest removing these areas with a 'maximum Pleistocene ice extent mask' from the Pliocene results, similarly to what is also done for the LGM. Both masks should be highlighted in another color than the background grey on Fig. 6 to make it more apparent. It is important to also show them on the FCI difference maps for the relevant time-slices (Fig. 7-10), so you don't compare FCI for regions within and outside of ice-sheets for different time slices. The latter would also eliminate the problem with sentences in e.g., line 306-307 and 317-318, where you seem to be unsure about whether FCI-differences result from ice cover during LGM or not.

This is a very valid and important concern. We addressed this as follows: The areas which experienced Pleistocene glaciation have been removed from the Pliocene results of all the three models. The figures (including captions) i.e. Fig. 6-10 and supplement Fig. 1 and 2 have been updated accordingly in the revised manuscript.

The glacier mask is applied and highlighted in FCI results (with a different color) for all the models (i.e., Fig. 6, 7 and Supplement Fig. 1 and 2) and FCI difference maps (i.e. Fig. 8-10), following the reviewer's suggestions. Hence, we no longer compare FCI for regions within and outside ice-sheets in the revised manuscript.

2. Your soil thickness data seem to saturate/max out at ~1 m (fig. 1). Are these minima estimates? It is not clear to me how you handle soils  $\geq 1$  m in the FCI model, or if you exclude these (extensive) regions. I would also like to see a discussion on how the uncertainties and coarse spatial resolution of the soil data may influence the modelled FCI on a sub-grid scale.

We consider the top soil (usually  $\leq 1$  m deep) in the FCI models and hence used the dataset from World Harmonized Soil Database (HWSD) v1.2 (Wieder, 2014) for present day. We do not explicitly define regolith and hence the strata below the top-soil is considered as bedrock in the first order estimation. However, future regional (or local) studies may include deeper soil depths preferably at finer spatial resolution, and extensive lithological information.

A discussion on the influence of uncertainties and coarse spatial resolution of the soil data on the modeled FCI on a sub-grid scale has been added in the model limitations (section 5.5) revised manuscript (lines 526-531).

3. I fail to see the relevance of the comparison to permafrost extent, and suggest cutting these sections out of the paper (Sec. 3.3, Sec 5.4.2, and Fig. 11+12).

We agree that the sections and figures relating FCI to permafrost extent does not add much insight into the discussion section and hence sec. 3.3, 5.4.2 and Fig. 11 and 12 are removed from the revised manuscript.

4. The discussion includes a number of 'predictions' that 'confirms' or 'agrees with' the models (e.g., line 287-288, line 429). These statements appear circular since your results are based on the same models, and does not really add anything new compared to reading the original papers. I suggest that you spend more space on comparing the models and testing the effect of the underlying assumptions in the main paper. For example: it is disputed whether the penalty functions that make FCI depend on distance to water give a better representation of the frost cracking process or not. Since you have gone through the trouble of implementing all three models, it would be interesting to use them to evaluate what predictions about global frost cracking the different choices result in. For example, you could test the effect of the penalty function by running models with and without the postulated influence on FCI, but maintaining the influence of porous (wet) soil on the temperature-profiles. Similarly, your section 5.4.1. would be better framed as an evaluation/discussion of the assumptions behind the different models, rather than evaluating your results directly. At present this section does not really add something new that is not in the original papers, which is why everything ends up being in agreement with your results.

We have updated the discussion section 5.3 to not directly compare our results with previous studies but rather compare the first order (global) trend of FCI with existing observations. Furthermore, we followed your advice to give more room in discussion to the importance of the penalty function. Specifically, we added a section in model results (section 4.2) to present the results for model 3 without the penalty function. We observed that the FCI trends were similar to Model 2 output (FCI as a function of temperature gradient if water is available at either boundary). The globally summed up FCI estimates (with inclusion of penalty function) were in agreement with studies on global weathering fluxes from LGM to present, which indicates 20% higher global weathering rates during LGM (than in present day). We concluded that our results speak in favor of the importance of the penalty function for global scale estimates of FCI. Thank you for the suggested change.

5. Section 4 and 5.1-5.3 and Fig. 7-10. These sections are rather long and hard to read. Please try to condense the most important lessons. I suggest referring to Fig. 8-10 as part of your global discussion in replacement of Sec. 5.3. Perhaps you could even consider showing the FCI-difference panels grouped by time-slice (e.g., PI-MH) instead of region, and then showing the regional details as sub-panels (b-d) to each global model (a) in each figure. This would also reduce the number of figures by one.

Thank you for the comment about the length of section 4 and 5.1-5.3. These have been simplified and reduced to condense the most important findings in the revised manuscript. Section 5.3 is

replaced and combined with section 5.2 (global analysis) following the updating of Fig. 8-10 as per above suggestion.

6. Consider calculating a globally summed FCI to highlight what periods frost cracking globally are more important to surface processes.

Thank you for that suggestion. We believe this is a good way to get additional important lessons out of our study. We have added a paragraph in discussion (section 5.1) (lines 365-383) in the revised manuscript to elaborate on above mentioned suggestion.

## **Figures, Tables**

Table 2: Too many digits?

The digits have been rounded off with no decimal values in Table 2.

Fig. 11+12: Stippled black line very hard to see.

The figures have been removed from the main text following the above suggestion (pt. 3 of reviewer's comments).

## **Line specific comments**

I. 20: 'In contrast' – these sentences does not really contrast

Removed 'In contrast' from line 21.

I. 26: Consider removing 'long ()'

Removed long () in line 28.

I. 29-31: Not so clear why vegetation is considered indirect, but other surface processes are considered direct.

This distinction may indeed be somewhat arbitrary after all. We revised the sentence (lines 31-35 in revised manuscript) to simply that that climate affects erosion through changes in vegetation or other said processes.

I. 70: 'Europe' is not an orogen

Line 79: We removed this sentence, since we simply focus our discussion on specific regions (hosting mountainous terrain), but do not conduct a separate analysis.

I. 74: 'and soil' read strange here

Line 83: 'and soil' has been changed to 'and soil dataset'

I. 96-98: I don't understand the reference soil depth information – consider to cut it unless it is relevant enough to explain in more detail?

Line 122: The reference soil depth information has been removed in the revised manuscript.

I. 145: I would not say more complete, but certainly more complex. It is disputed whether the penalty functions (or the ad hoc choice of parameter values in different media) give a better representation of the frost cracking process than a simpler model.

Line 178: 'more complete' has been changed to 'complex'. We have added a section in Results (section 4.2) and Discussion (section 5.1) to elaborate and discuss the sensitivity of Model 3 (Andersen et al., 2015) to penalty functions, in estimation of FCI at global scale.

I. 181-182: This seems redundant. No need to mention it in each section, and twice in this section (also I. 197).

Removed redundant sentences from line 220 and 235.

I. 186: In the case 'of' permafrost

Line 223: corrected from 'if permafrost' to 'of permafrost'.

I. 187: Fig. 3, not 2

Line 225: corrected from Fig. 2 to Fig. 3

I. 275: discussion 'of' regional variations

Line 352: added 'of' between 'discussion' and 'regional variations'

I. 484: frost cracking 'occurs' at lower latitudes

Line 570: added 'occurs' between 'frost cracking' and 'at lower latitudes'

# 1 The Effects of Late Cenozoic Climate Change on the Global 2 Distribution of Frost Cracking

3 Hemanti Sharma<sup>1</sup>, Sebastian G. Mutz<sup>1</sup>, Todd A. Ehlers<sup>1\*</sup>

4 <sup>1</sup>Department of Geosciences, University of Tuebingen, Tuebingen, 72076, Germany

5 \*Correspondence to: Todd A. Ehlers (todd.ehlers@uni-tuebingen.de)

6 **Abstract.** Frost cracking is a dominant mechanical weathering phenomenon facilitating the breakdown of bedrock  
7 in periglacial regions. Despite recent advances in understanding frost cracking processes, few studies have  
8 addressed how global climate change over the Late Cenozoic may have impacted spatial variations in frost  
9 cracking intensity. In this study, we estimate global changes in frost cracking intensity (FCI) by segregation ice  
10 growth. Existing process-based models of FCI are applied in combination with soil thickness data from the  
11 Harmonized World Soil Database. Temporal and spatial variations in FCI are predicted using surface temperatures  
12 changes obtained from ECHAM5 general circulation model simulations conducted for four different paleoclimate  
13 time-slices. Time-slices considered include Pre-Industrial (~1850 CE, PI), Mid-Holocene (~6 ka, MH), Last  
14 Glacial Maximum (~21 ka, LGM) and Pliocene (~3 Ma, PLIO) times. Results indicate for all paleoclimate time  
15 slices that frost cracking was most prevalent (relative to PI times) in the mid to high latitude regions, as well as  
16 high-elevation lower latitudes areas such the Himalayas, Tibet, European Alps, the Japanese Alps, the USA Rocky  
17 Mountains, and the Andes Mountains. The smallest deviations in frost cracking (relative to PI conditions) were  
18 observed in the MH simulation, which yielded slightly higher FCI values in most of the areas. In contrast, larger  
19 deviations were observed in the simulations of the colder climate (LGM) and warmer climate (PLIO). Our results  
20 indicate that the impact of climate change on frost cracking was most severe during the PI – LGM period due to  
21 higher differences in temperatures and glaciation at higher latitudes. **The PLIO results indicate low FCI in the**  
22 **Andes and higher values of FCI in Greenland and Canada due to the diminished extent of glaciation in the warmer**  
23 **PLIO climate.**

Deleted: In contrast, the

24 **Keywords:** Climate Change, frost cracking, physical weathering, Pre-Industrial, Mid-Holocene, Last Glacial  
25 Maximum, Pliocene

## 26 1. Introduction

27 Climate change, mountain building, and erosion are closely linked over different spatial and temporal scales (e.g.  
28 Whipple, 2009; Adams et al., 2020). Over **million year timescales, mountain building alters global climate by**  
29 introducing physical obstacles to atmospheric flow (Raymo and Ruddiman, 1992) that influences regional  
30 temperatures and precipitation (Botsyun et al., 2020; Ehlers and Poulsen, 2009; Mutz et al., 2018; Mutz and Ehlers,  
31 2019). Over decadal to million-year time scales, climate change impacts the erosion of mountains **in several ways,**  
32 **such as** through the modification of vegetation cover (e.g. Acosta et al., 2015; Schmid et al., 2018; Werner et al.,  
33 2018; Starke et al., 2020; **Schaller and Ehlers, 2022**), and **through its influence on physical and chemical**  
34 weathering processes, as well as glacial, fluvial and hillslope erosion (e.g. Valla et al., 2011; Herman et al., 2013;  
35 Lease and Ehlers, 2013; Perron, 2017). Climate change from the Late Cenozoic to present has played an important

Deleted: long (

Deleted: )

Deleted: both indirectly, e.g.

Deleted: directly

41 role in eroding mountain topography and lowland sedimentation (Hasler et al., 2011; Herman and Champagnac,  
42 2016; Marshall et al., 2015; Peizhen et al., 2001; Rangwala and Miller, 2012). Climate change influences surface  
43 processes through not only precipitation changes, but also through seasonal temperature changes that affect  
44 physical weathering mechanisms, such as frost cracking (Anderson, 1998; Delunel et al., 2010; Hales and Roering,  
45 2007; Walder and Hallet, 1985). Critical cracking occurs when the pressure of freezing (and expanding) water in  
46 pore walls or fractures exceeds the cohesive strength of the porous media and causes cracks to propagate  
47 (Davidson and Nye, 1985). However, subcritical cracking can also occur without exceeding thresholds (Eppes  
48 and Keanini, 2017). Frost cracking is a dominant mechanism of weathering in periglacial regions (Marshall et al.,  
49 2015), and typically occurs at latitudes greater than 30°N and 30°S or in high elevations.  
50 Previous field studies of frost cracking in mountain regions includes studies in, for example, the Japanese Alps  
51 (Matsuoka, 2001), Southern Alps of New Zealand (Hales and Roering, 2009), Swiss Alps (Amitrano et al., 2012;  
52 Girard et al., 2013; Matsuoka, 2008; Messenzehl et al., 2017), French Western Alps (Delunel et al., 2010), Italian  
53 Alps (Savi et al., 2015), Eastern Alps (Rode et al., 2016), Austrian Alps (Kellerer-Pirklbauer, 2017), Oregon  
54 (Marshall et al., 2015; Rempel et al., 2016), and the Rocky Mountains, USA (Anderson, 1998). These studies  
55 demonstrated clear relationships between changes in near surface air temperatures and frost cracking. Various  
56 models have also been developed to estimate frost cracking intensity (FCI) using mean annual air temperatures  
57 (MAT) (Andersen et al., 2015; Anderson, 1998; Anderson et al., 2013; Hales and Roering, 2007; Marshall et al.,  
58 2015) and in some cases, with the additional consideration of sediment thickness variations over bedrock  
59 (Andersen et al., 2015; Anderson et al., 2013). These studies document the importance of time spent in the frost  
60 cracking window (FCW) for the frost-cracking intensity (FCI) of a given area. The assumption of FCW is based  
61 on the premise that frost cracking occurs in response to segregation ice growth in bedrock when subsurface  
62 temperatures are between -8 °C and -3 °C (Anderson, 1998). However, this assumption is not supported by  
63 physical models (e.g. Walder and Hallet, 1985), field data (e.g. Girard et al., 2013; Draebing et al., 2017) or lab  
64 simulations (e.g. Murton et al., 2016). The FCW depends on rock strength and crack geometry (Walder and Hallet,  
65 1985), and thus spatial variations are expected due to lithological changes. More complex models consider near  
66 surface thermal gradients as a proxy of the frost cracking intensity for segregation ice growth, as well as the effects  
67 of overlying sediment layer thickness on frost cracking (Andersen et al., 2015).  
68 The previous studies provide insight into not only observed regional variations in frost cracking, but also some of  
69 the key processes required for predicting frost cracking intensity. However, despite recognition that Late Cenozoic  
70 global climate change impacts surface processes (e.g. Mutz et al., 2018; Mutz and Ehlers, 2019) and frost-cracking  
71 intensity (e.g. Marshall et al., 2015), to the best of our knowledge, no study has taken full advantage of climate  
72 change predictions in conjunction with a process-based understanding of the spatiotemporal variations in frost  
73 cracking on a global scale. This study builds upon previous work by estimating the global response in FCI to  
74 different end-member climate states. Here, we complement previous work on the effects of climate on surface  
75 processes by addressing the following hypothesis: If Late Cenozoic global climate change resulted in latitudinal  
76 variations in ground surface temperatures, then the intensity of frost cracking should temporally and spatially vary  
77 in such a way that leads to the occurrence of more intense frost cracking at lower latitudes during colder climates.  
78 We do this by coupling existing frost-cracking models to high-resolution paleoclimate General Circulation Model  
79 (GCM) simulations (Mutz et al., 2018). More specifically we apply three different frost-cracking models that are  
80 driven by predicted surface temperature changes from GCM time-slice experiments including (a) the Pliocene

Deleted: Frost

Deleted: Here, we complement previous work on the effects of climate on surface processes by addressing the following hypothesis: If Late Cenozoic global climate change resulted in latitudinal variations in ground surface temperatures, then the intensity of frost cracking should temporally and spatially vary in such a way that leads to the occurrence of more intense frost cracking at lower latitudes during colder climates.

Deleted: process-based

Deleted: -

Deleted: frost-cracking window

Deleted: ; Walder and Hallet, 1985

94 (~3 Ma, PLIO), considered an analog for Earth’s potential future due to anthropogenic climate change, (b) the  
 95 Last Glacial Maximum (~21 ka, LGM), covering a full glacial period, (c) the Mid-Holocene (~6 ka, MH) climate  
 96 optimum, and (d) Pre-Industrial (~1850 CE, PI) conditions before the onset of significant anthropogenic  
 97 disturbances to climate.

**Deleted:** In addition to a global analysis, we investigate how FCI varies for selected orogens including the Himalaya-Tibet, European Alps and the Andes.

98 **2. Data**

99 This manuscript builds upon and uses paleoclimate model simulations we previously published for different time  
 100 periods (Mutz et al., 2018; Mutz and Ehlers, 2019). The output from those simulations was used for new  
 101 calculations of FCI described below. More specifically, the climate and soil dataset used for this study includes  
 102 simulated daily land surface temperatures (obtained from the Mutz et al. (2018) simulations) for different  
 103 paleoclimatic time-slice experiments (PI, MH, LGM and PLIO) conducted with the GCM ECHAM5 simulations,  
 104 and soil thickness data (Wieder, 2014). Due to the lack of paleo soil thickness data, global variations in soil  
 105 thickness are assumed to be uniform between all time-slices investigated. The reader is advised that this  
 106 assumption has limitations and would introduce uncertainty in the model results as past weathering would alter  
 107 soil thickness and hence influence further weathering. However, as the main goal of this study is to simulate and  
 108 analyze the climate change effect for global FCI changes in different palaeoenvironmental conditions, we keep  
 109 the soil thickness constant. In addition, there are no data sets available for past soil thicknesses that would allow  
 110 circumventing the approach used here. Given this, we use a present-day dataset for soil thickness due to the  
 111 absence of paleo soil data.

**Deleted:** have

112 The ECHAM5 paleoclimate simulations were conducted at a high spatial resolution (T159, corresponding roughly  
 113 to a 80km x 80km horizontal grid at the equator) and 31 vertical levels (to 10hPa). ECHAM5 was developed at  
 114 the Max Planck Institute for Meteorology (Roeckner et al., 2003). It is based on the spectral weather forecast  
 115 model of ECMWF (Simmons et al., 1989) and is a well-established tool in modern and paleoclimate studies. The  
 116 ECHAM5 paleoclimate simulations by Mutz et al. (2018) were driven with time-slice specific boundary  
 117 conditions derived from multiple modeling initiatives and paleogeographic, paleoenvironmental and vegetation  
 118 reconstruction projects (see Table 1). Details about the boundary conditions and prevailing climates for specific  
 119 time-slices (PI, MH, LGM and PLIO) are provided in Mutz et al. (2018). Each simulated time-slice resulted in 17  
 120 simulated model years, where the first two years contained model spin up effects and were discarded. The  
 121 remaining 15 years of simulated climate were in dynamic equilibrium with the prescribed boundary conditions  
 122 and used for our analysis.

123

124

125 **Table 1. Boundary Conditions of the paleoclimate simulations (Mutz et al., 2018).**

| Paleoclimate Simulations | Boundary Conditions  |
|--------------------------|--|
| PI (~ 1850)              | <ul style="list-style-type: none"> <li>• Sea-Surface temperatures (SST) and sea-ice concentrations (SIC) were sourced from transient coupled ocean-atmosphere simulations (Dietrich et al., 2013; Lorenz and Lohmann, 2004)</li> <li>• Green-house gas (GHG) concentrations (Dietrich et al., 2013) were obtained from ice-core-based reconstructions of CO<sub>2</sub> (Etheridge et al., 1996), CH<sub>4</sub> (Etheridge et al., 1998), and N<sub>2</sub>O (Sowers et al., 2003)</li> </ul> |

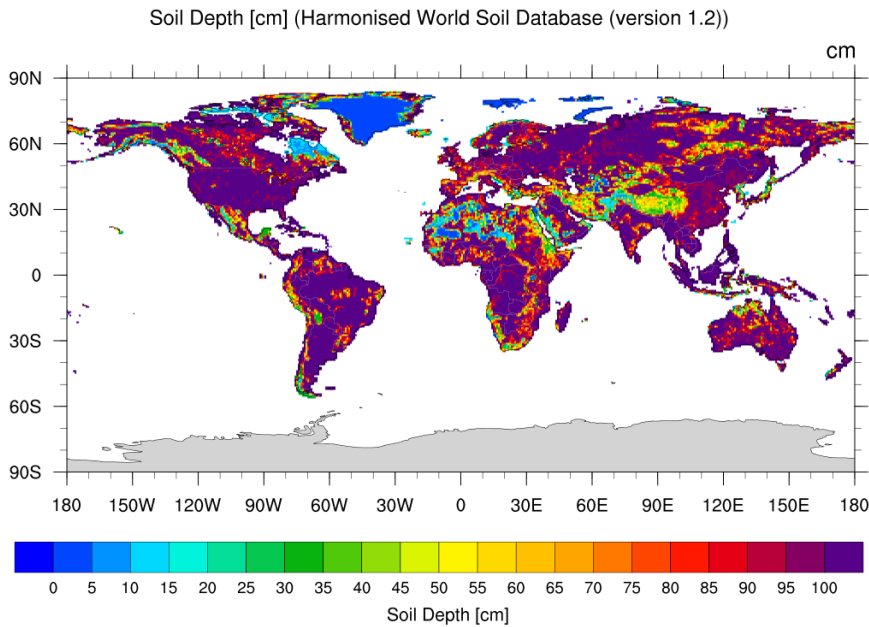


|                      |   |
|----------------------|---|
| <b>MH (~ 6 ka)</b>   | <ul style="list-style-type: none"> <li>• SST and SIC are derived from a transient, low resolution, coupled atmosphere-ocean simulation of the mid (6 ka) Holocene (Lohmann et al., 2013; Wei and Lohmann, 2012)</li> <li>• GHG concentrations (Dietrich et al., 2013) are obtained from ice-core-based reconstructions of CO<sub>2</sub> (Etheridge et al., 1996), CH<sub>4</sub> (Etheridge et al., 1998), and N<sub>2</sub>O (Sowers et al., 2003)</li> <li>• Global vegetation maps are based on plant functional types maps by the BIOME 6000 / Palaeovegetation Mapping Project (Prentice et al., 2000; Harrison et al., 2001; Bigelow et al., 2003; Pickett et al., 2004) and model predictions by Arnold et al. (2009)</li> <li>• Orbital parameters from Dietrich et al., (2013)</li> </ul> |
| <b>LGM (~ 21 ka)</b> | <ul style="list-style-type: none"> <li>• Land-sea distribution and ice sheet extent and thickness are based on the PMIP III guidelines (Abe-Ouchi et al., 2015)</li> <li>• SST and SIC are based on GLAMAP (Sarnthein et al., 2003) and CLIMAP (CLIMAP group members, 1981) reconstructions</li> <li>• GHGs concentrations are prescribed following Otto-Bliesner et al. (2006)</li> <li>• Global vegetation maps are based on plant functional types maps by the BIOME 6000 / Palaeovegetation Mapping Project (Prentice et al., 2000; Harrison et al., 2001; Bigelow et al., 2003; Pickett et al., 2004) and model predictions by Arnold et al. (2009)</li> <li>• Orbital parameters from Dietrich et al., (2013)</li> </ul>  |
| <b>PLIO (~ 3 Ma)</b> | <ul style="list-style-type: none"> <li>• Surface conditions (SST, SIC, sea land mask, topography and ice cover), GHG concentrations and orbital parameters are obtained from the PRISM project (Haywood et al., 2010; Sohl et al., 2009; Dowsett et al., 2010)</li> <li>• PRISM vegetation reconstruction converted to ECHAM5 compatible plant functional types following Stepanek and Lohmann (2012)</li> </ul>  |

130

131 \* (SST: Sea Surface Temperature; SIC: Sea Ice Concentration; GHG: Greenhouse Gas; PMIP III: Paleoclimate

132 Modelling Intercomparison Project, phase 3; PRISM: Pliocene Research, Interpretation and Synoptic Mapping)



133

134 **Figure 1. Soil depth map from the Harmonized World Soil Database (HWSD, version 1.2) used in this study**  
 135 **(Wieder, 2014). Due to the paucity of some data inputs for paleoclimate time-slices (e.g. soil thickness, rock**  
 136 **properties, hydrology, etc.), the simulations assume present day values.**

137 Soil thickness data was obtained from the re-gridded Harmonized World Soil Database (HWSD) v1.2 (Wieder,  
 138 2014) which has a 0.05-degree spatial resolution and depths ranging from 0 m to 1 m (Fig. 1). The above soil  
 139 thickness data was upscaled to match the spatial resolution of the ECHAM5 paleoclimate simulations (T159, ca.  
 140 80km x 80km).

**Deleted:** In the dataset, reference soil depth for all the soil units is set to 100 cm, except for Rendzinas and Rankers of FAO-74 and Leptosols of FAO-90, where the reference soil depth is set to 30 cm, and Lithosols of FAO-74 and Lithic Leptosols of FAO-90, where it is set to 10 cm (Wieder, 2014).

141 **3. Methods**

**Formatted:** Indent: Left: 0 cm, Hanging: 0.63 cm

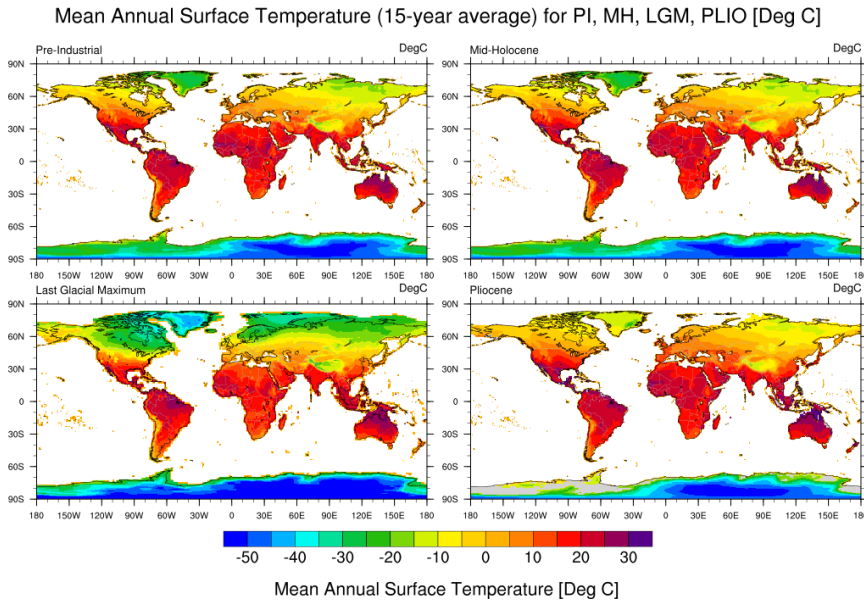
142 In this section we present the pre-processing of GCM paleo-temperature data for the calculation of mean annual  
 143 temperatures (MAT) and the half amplitude of annual temperature variations (Ta). This is followed by the  
 144 description of the models (simpler to complex) that were applied to generate first order (global) estimation of  
 145 annual depth integrated FCI for selected Cenozoic time-slices.

**Deleted:** Soil thickness data was obtained from the re-gridded Harmonized World Soil Database (HWSD) v1.2 (Wieder, 2014) which has a 0.05-degree spatial resolution and depths ranging from 0 m to 1 m (Fig. 1). In the dataset, reference soil depth for all the soil units is set to 100 cm, except for Rendzinas and Rankers of FAO-74 and Leptosols of FAO-90, where the reference soil depth is set to 30 cm, and Lithosols of FAO-74 and Lithic Leptosols of FAO-90, where it is set to 10 cm (Wieder, 2014). The above soil thickness data was upscaled to match the spatial resolution of the ECHAM5 paleoclimate simulations (T159, ca. 80km x 80km). [Methods](#)

146 **3.1. Pre-processing of GCM simulation temperature data**

147 We calculated the mean annual land surface temperatures (MAT) to serve as input for subsequent calculations  
 148 and a reference for differences in global paleoclimate. The MAT's for the paleoclimate GCM experiments (PLIO,  
 149 LGM, MH, and PI) were calculated (Fig. 2) from each of the simulations' 15 years of daily land surface

168 temperature values. In addition, the half amplitude of annual surface temperature variations (Ta) was extracted at  
 169 all surface grid locations for all years (Fig. 3). We use the MAT for ground surface temperature in subsequent  
 170 calculations, following Anderson et al., (2013), Marshall et al., (2015), and Rempel et al., (2016) . The maxima  
 171 and minima for global average MAT's and Ta's for all the time-slices are shown in Table 2.



172

173 **Figure 2.** Mean Annual Surface Temperature maps (15-year average) from the ECHAM5 GCM simulations for the  
 174 Pre-Industrial (top-left), Mid-Holocene (top-right), Last Glacial Maximum (bottom-left), and mid-Pliocene  
 175 (right) (unit: °C). These are calculated from GCM simulation output of Mutz et al. (2018) and Mutz and Ehlers (2019).  
 176

177 **Table 2.** MAT and Ta (for ground surface temperature) for Pre-Industrial, Mid-Holocene, Last Glacial Maximum and  
 178 Pliocene simulations.

| Time-slices<br>(Paleoclimate Simulations) | MAT (°C) |         | Ta (°C) |         |
|---|----------|---------|---------|---------|
|   | Minimum  | Maximum | Minimum | Maximum |
| Pre-Industrial (~ 1850)                   | -58      | 34      | 0       | 39      |
| Mid-Holocene (~ 6 ka)                     | -58      | 35      | 0       | 40      |
| Last Glacial Maximum (~21 ka)             | -67      | 39      | 0       | 42      |
| Pliocene (~ 3 Ma)                         | -56      | 48      | 0       | 43      |

179

180 The calculation of temporally varying sub-surface temperatures follows the approach of Hales and Roering (2007)  
 181 and uses the analytical solution for the one-dimensional heat conduction equation (Turcotte and Schubert, 2014)

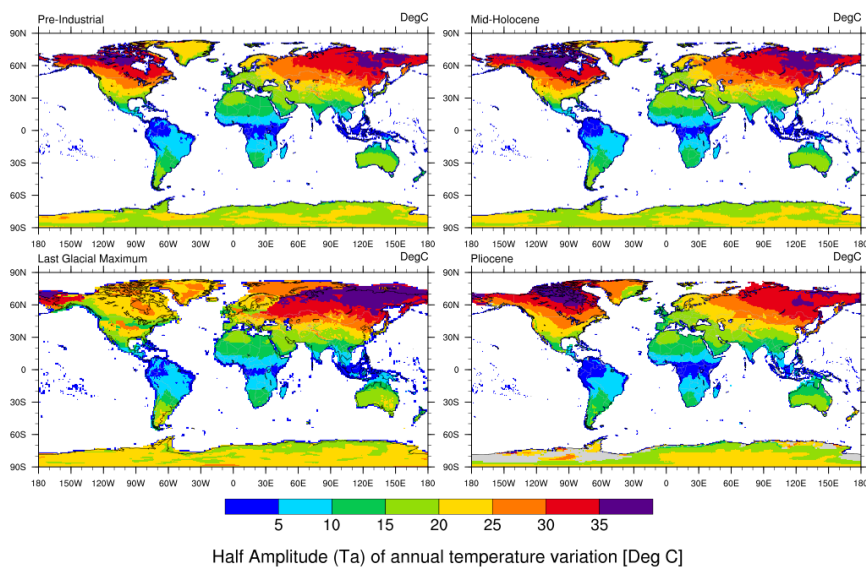
- Deleted: .31
- Deleted: .03
- Deleted: 38.64
- Deleted: .50
- Deleted: .19
- Deleted: 39.6
- Deleted: 66.93
- Deleted: 38.74
- Deleted: 41.74
- Deleted: .20
- Deleted: .23
- Deleted: .21

194 forced with daily temperatures following sinusoidal variations. While daily paleo-temperatures can be obtained  
 195 from Mutz et al. (2018), the daily variations produced by the GCM cannot be validated as well as seasonal or  
 196 annual means. To avoid overinterpretation of the GCM simulations, we refrained from using daily paleo-  
 197 temperatures from Mutz et al. (2018) and instead use sinusoidal daily temperatures. Temperature variations with  
 198 depth and time were calculated at each GCM grid point as:

$$199 \quad T(z, t) = MAT + Ta \cdot e^{-z \sqrt{\frac{\pi}{\alpha P_y}}} \cdot \sin\left(\frac{2\pi t}{P_y} - z \sqrt{\frac{\pi}{\alpha P_y}}\right) \quad (1)$$

200 where,  $T$  represents daily subsurface temperature at depth  $z$  (m) and time  $t$  (days in a year),  $MAT$  and  $Ta$  represent  
 201 mean annual surface temperature and half amplitude of annual temperature variation respectively,  $P_y$  is the period  
 202 of the sinusoidal cycle (1 year), and  $\alpha$  is the thermal diffusivity. Thermal diffusivity values near the Earth's surface  
 203 can range from  $1 - 2 \times 10^{-6} m^2 s^{-1}$  for most rocks (Anderson, 1998) and range between  $7 -$   
 204  $10 \times 10^{-7} m^2 s^{-1}$  for other Earth materials comprising the overlying sediment layer (Eppelbaum et al., 2014).  
 205 In this study, we used a thermal diffusivity of  $1.5 \times 10^{-6} m^2 s^{-1}$  for bedrock and  $8 \times 10^{-7} m^2 s^{-1}$  for the  
 206 overlying sediment layer. The maximum depth investigated here is 20 m, as it is slightly deeper than the maximum  
 207 frost penetration depth of  $\sim 14$  m reported by (Hales and Roering, 2007).

Half Amplitude of Annual Temperature Variation (15-year average) for MH, LGM, PLIO [Deg C]



208

209 **Figure 3. Half Amplitude of Annual Temperature Variation (15-year average) for the Pre-Industrial (top-left), Mid-**  
 210 **Holocene (top-right), Last Glacial Maximum (bottom-left), and Pliocene (bottom-right) (unit: °C). These are calculated**  
 211 **from GCM simulation output of Mutz et al., (2018) and Mutz and Ehlers (2019).**

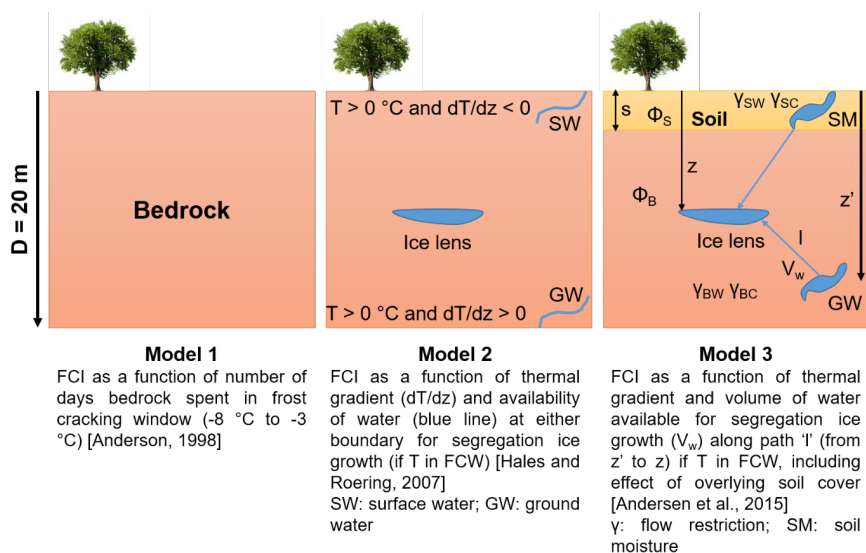
212 The calculation of subsurface temperatures was discretized into 200 depth intervals from the surface to the  
 213 maximum depth of 20 m. Smaller depth intervals (~1 cm) were used near the surface and large intervals (~20 cm)  
 214 at greater depths, because the FCI is expected to change most dramatically near the surface and dampen with  
 215 depth due to thermal diffusion (Andersen et al., 2015).

216 **3.2. Estimation of Frost Cracking Intensity**

217 We applied three different approaches (models) with different levels of complexity to estimate global variations  
 218 in frost cracking during different past climates (Fig 4; Andersen et al., 2015; Anderson, 1998; Hales and Roering,  
 219 2007). The models use predicted ground surface temperatures from each grid cell in the GCM to calculate  
 220 subsurface temperatures and FCI. We then calculate differences between the FCI from the PI reference simulation  
 221 and the FCI predicted for the PLIO, LGM and MH time-slices to assess relative change in FCI over the Late  
 222 Cenozoic. The conceptual diagram (Fig. 4) illustrates differences in the models used in our study, which are  
 223 discussed in detail in sections 3.2.1 - 3.2.3. Models 1-3 successively increase in complexity and consider more  
 224 factors. The approach of Andersen et al., (2015), referred to here as Model 3, is the most recent and **complex** in  
 225 its consideration of the processes (e.g. effect of soil-cover on FCI) that are relevant for frost cracking. Given this,  
 226 we focus our presentation of results in the main text here on Model 3, but for completeness describe below  
 227 differences of Model 3 from earlier Models (1-2). For brevity, results from the earlier models are presented in the  
 228 supplementary material. A flowchart illustrating our methods is presented in Fig. 5. Similar to previous studies,  
 229 the hydrogeological properties of the bedrock (i.e. infiltration, water saturation, porosity and permeability) are  
 230 ignored in this study. This approach provides a simplified means for estimating the FCI for underlying bedrock at  
 231 a global scale.

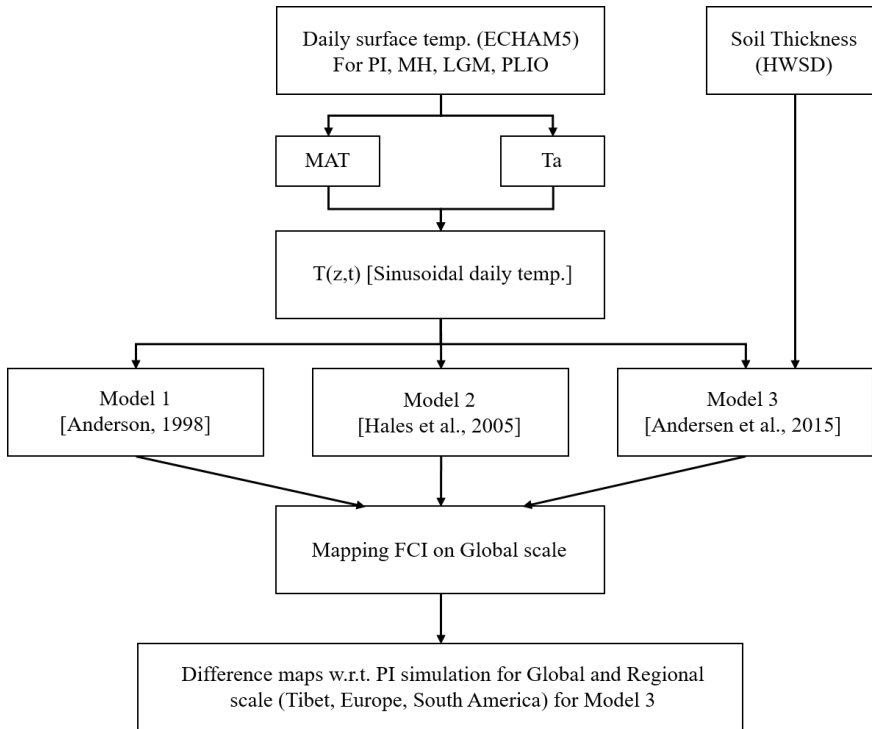
Deleted: complete

232



233

235 Figure 4. Conceptual diagram of the models (1, 2, and 3) used for estimating FCI (T: temperature; dT/dz: thermal  
 236 gradient; SW: surface water; GW: groundwater; SM: soil moisture; s: sediment thickness;  $\phi_S$ : soil porosity (0.02);  $\phi_B$ :  
 237 bedrock porosity (0.3)).



238  
 239 Figure 5. Flowchart describing the methods used in the study based on daily surface temperature simulated by the  
 240 ECHAM GCM. and soil thickness data from HWSD v1.2. Abbreviations include: MAT - mean annual temperature;  
 241 Ta - half amplitude of annual temperature variation; T (z, t) - subsurface temperature at depth z and time t; FCI - frost  
 242 cracking intensity.

243 **3.2.1. Model 1: Frost cracking intensity as a function of time spent in the frost cracking window (FCW)**

244 Model 1 represents the simplest approach and applies the method of Anderson (1998). In our application of this  
 245 model, we use a more representative thermal diffusivity value for rocks of  $1.5 \times 10^{-7} m^2 s^{-1}$ , because the  
 246 previous study was specific to granitic bedrock and applied a diffusivity specific to that. Furthermore, the  
 247 boundary conditions of a low rock surface albedo ( $\leq 0.1$ ) and presence of a high atmospheric transmissivity ( $\geq$   
 248 0.9) on the surface were relaxed, as surface temperatures were used in our study instead of near-surface air  
 249 temperatures.

250 For our implementation of model 1, we applied equation 1 for sinusoidal varying daily temperatures at the surface,  
 251 and calculated temperatures up to 20 m depth. The number of days spent in the **FCW** ( $-8^{\circ}\text{C}$  to  $-3^{\circ}\text{C}$ ) for each  
 252 depth interval were calculated over a period of 1 year for all time slices (PI, MH, LGM and PLIO):

$$253 \quad FCI(z) = \begin{cases} N(z), & \text{if } -8^{\circ}\text{C} < T(z, t) < -3^{\circ}\text{C} \\ 0, & \text{else} \end{cases} \quad (2)$$

254 where  $FCI(z)$  is referred to the frost cracking intensity at depth  $z$ .  $N(z)$  indicates the number of days the bedrock  
 255 (at depth  $z$ ) spends in the **FCW** over a period of 1 year.

256 Estimation of frost cracking intensity for each location included depth averaging of the FCI such that:

$$257 \quad \hat{FCI} = \frac{1}{D} \int_0^D FCI(z) dz \quad (3)$$

258 where  $\hat{FCI}$  is the integrated frost cracking intensity to a depth of  $D = 20\text{ m}$ . The unit of integrated frost cracking  
 259 intensity in this model is *Days*. The FCI values are calculated for all model years separately and then averaged  
 260 over the total time (15 years) for each paleoclimate time-slice.

### 261 3.2.2. Model 2: Frost cracking intensity as a function of subsurface thermal gradients

262 Model 2 applies the approach of Hales and Roering (2007) to estimate FCI using climate change driven variations  
 263 in subsurface thermal gradients. This approach extends the work of Anderson (1998) with the additional  
 264 consideration of segregation ice growth. Segregated ice growth is attributed to the migration of liquid water to  
 265 colder regions in shallow bedrock, accumulating in localized zones to form ice lenses inducing weathering  
 266 (Walder and Hallet, 1985).

267 To facilitate ice segregation growth, the model assumes the availability of liquid water ( $T > 0^{\circ}\text{C}$ ) at either  
 268 boundary ( $z = 0\text{ m}$  or  $z = 20\text{ m}$ ), with a negative thermal gradient for a positive surface temperature, and a positive  
 269 thermal gradient for the positive lower boundary ( $z = 20\text{ m}$ ) temperature. This implementation supports frost  
 270 cracking in the bedrock with temperatures between  $-8^{\circ}\text{C}$  and  $-3^{\circ}\text{C}$  (Hallet et al., 1991). In the case of permafrost  
 271 areas, MAT is always negative, but as sinusoidal  $T(z, t)$  is calculated based on MAT and  $T_a$ , a positive  $T (> 0^{\circ}\text{C})$   
 272 may occur during warmer days of the year. In addition,  $T_a$  is higher for higher latitudes (Fig. 3), which are more  
 273 prone to frost cracking.

274 The model is described as follows:

$$275 \quad FCI(z, t) = \begin{cases} \left| \frac{dT}{dz} \right| (z, t), & \text{if } -8^{\circ}\text{C} < T(z, t) < -3^{\circ}\text{C} \\ 0, & \text{else} \end{cases} \quad (4)$$

$$276 \quad \hat{FCI} = \int_0^D \int_0^{Py} FCI(z, t) dt dz \quad (5)$$

277 where  $FCI(z, t)$  is the frost cracking intensity at depth  $z$  and time  $t$ . It is an index for the absolute value of the  
 278 thermal gradient at that particular depth and time that fulfils the conditions defined above.

279 In equation 5,  $\hat{FCI}$  represents the integrated FCI for a geographic location. More specifically, the FCI is integrated  
 280 over one year at each depth and then integrated for all depth elements.  $D$  represents depth (20 m),  $Py$  is a period

Deleted: frost cracking window

Deleted: frost cracking window

Deleted: For this approach, we applied equation 1 for temperatures to 20 m depth and for a time duration of 1 year. Again, FCI is computed for each of the 15 years in the GCM simulation and averaged.

Deleted: if

Deleted: 2

289 of the sinusoid (1 year),  $dt$  is the time interval (1 day) and  $dz$  is the depth interval, as described in section 3.1. The  
 290 unit of integrated frost cracking intensity in this case is  $^{\circ}\text{C}\cdot\text{m}$ .

**Deleted:** It is calculated for each of the GCM model years and then averaged over the total time (15 years).

### 291 3.2.3. Model 3: Frost cracking intensity as a function of thermal gradients and sediment thickness

292 In the final (most complex) approach used in this study, the effect of an overlying soil layer (Fig. 1) is considered  
 293 in addition to the subsurface thermal gradient variations with depth. This model applies the approach of Andersen  
 294 et al. (2015), which extends the work of Hales and Roering (2007) and Anderson et al. (2013). The model  
 295 assumptions are similar to the previous approaches. For segregation ice growth, it additionally **considers** the  
 296 influence of the volume of water available in the proximity of an ice lens. The parameters used in Model 3 are  
 297 listed below (Table 3).

298 **Table 3. Input parameters for Model 3 (Andersen et al., 2015)**

| Symbol        | Description                      | Value                |
|---------------|----------------------------------|----------------------|
| $\Phi_s$      | Porosity of soil                 | 0.3                  |
| $\Phi_B$      | Porosity of bedrock              | 0.02                 |
| $\gamma_{sw}$ | Flow restriction in warm soil    | $1.0 \text{ m}^{-1}$ |
| $\gamma_{sc}$ | Flow restriction in cold soil    | $2.0 \text{ m}^{-1}$ |
| $\gamma_{BW}$ | Flow restriction in warm bedrock | $2.0 \text{ m}^{-1}$ |
| $\gamma_{BC}$ | Flow restriction in cold bedrock | $4.0 \text{ m}^{-1}$ |
| $V_{CW}$      | Critical water volume            | 0.04 m               |

299

300 In Model 3, frost cracking intensity is estimated as a product of the thermal gradient and volume of water available  
 301 ( $V_w$ ) for segregation ice growth at each depth element, such that:

$$302 \quad FCI(z, t) = \begin{cases} \left. \frac{dT}{dz}(z, t) \right| V_w(z), & \text{if } -8^{\circ}\text{C} < T(z, t) < -3^{\circ}\text{C} \\ 0, & \text{else} \end{cases} \quad (6)$$

303 where,  $FCI(z, t)$  is the frost cracking intensity in bedrock at depth  $z$  and time  $t$ , and  $V_w(z)$  is the volume of water  
 304 available for segregation ice growth.  $V_w(z)$  is estimated at each depth ( $z$ ) by integrating the occurrence of unfrozen  
 305 water along a path  $l$ , starting at depth  $z$  and following a positive thermal gradient towards the ice lens. The volume  
 306 of available water ( $V_w(z)$ ) and total flow restriction ( $\Gamma(z')$ ), between the depth of occurrence of water ( $z'$ ) and the  
 307 location of segregation ice growth ( $z$ ), are calculated using equations 7 and 8 respectively (Andersen et al., 2015):

$$308 \quad V_w(z) = \int_l \phi(z') w_f(z') e^{-\Gamma(z')} dz' \quad (7)$$

$$309 \quad \Gamma(z') = \int_z^{z'} \gamma(z'') dz'' \quad (8)$$

310 where,  $l$  is the distance from depth  $z$  to the surface, lower boundary, or an interface where the thermal gradient  
 311 changes sign (from positive to negative or vice versa). The penalty function  $e^{-\Gamma(z')}$  (Anderson et al., 2013) is a  
 312 function of the total flow restriction ( $\Gamma(z')$ ) at the depth  $z'$ . Since segregation ice growth is exhibited at sub-zero



315 temperatures (below  $-3^{\circ}\text{C}$ ) and liquid water is available at positive temperatures ( $T > 0^{\circ}\text{C}$ ), water must migrate  
 316 through a mixture of frozen and unfrozen soil or the bedrock. The variables  $\gamma_{\text{sw}}$ ,  $\gamma_{\text{sc}}$ ,  $\gamma_{\text{bw}}$ ,  $\gamma_{\text{bc}}$  (defined in Table  
 317 3) represent the flow restriction parameters and were used in the model to approximate a range of permeabilities  
 318 (Andersen et al., 2015), but do not explicitly simulate water transport. However, it is unclear if the inclusion of  
 319 the penalty function leads to a better representation of frost cracking processes. Therefore, we conducted two sets  
 320 experiments for Model 3 that were conducted with, and without, the penalty function and are presented in section  
 321 4.1 and 4.2, respectively.

322 The soil porosity ( $\phi_{\text{s}} = 0.3$ ) is assumed to be higher than that of bedrock ( $\phi_{\text{b}} = 0.02$ ).  $V_{\text{w}}(z)$  is expected to be high  
 323 due to the presence of unfrozen soil in the proximity of a frozen bedrock. Since Model 3 limits the positive effects  
 324 of  $V_{\text{w}}$  to a critical water volume  $V_{\text{cw}}$  (Table. 2, i.e., if  $V_{\text{w}} > V_{\text{cw}}$ , then  $V_{\text{w}} = V_{\text{cw}}$ ), the expected high ( $> V_{\text{cw}}$ )  
 325 values for  $V_{\text{w}}$  will not affect frost cracking any further.

326 Lastly, the integrated frost cracking intensity  $\overline{FCI}$  across Earth's terrestrial surface was calculated by depth  
 327 integration of the FCI averaged over a period of 1 year (Anderson et al., 2013):

$$328 \overline{FCI} = \frac{1}{Py} \int_0^{Py} \int_0^D FCI(z, t) dz dt \quad (9)$$

329 where,  $Py$  is 1 year and  $D$  is the maximum depth investigated (20 m). The unit of integrated FCI in this model is  
 330  $^{\circ}\text{Cm}$ . Integrated FCI is calculated for each of the GCM simulation's model years and then averaged over the  
 331 total number of years (15 years).

#### 332 4. Results

333 In the following, we document the general trends in the estimated FCI from Model 3 (Andersen et al., 2015) for  
 334 all the paleoclimate time-slices (PI, MH, LGM, PLIO) based on the coupling of the above models to GCM output  
 335 for these time slices. We present the results for the experiments conducted with and without the penalty function  
 336 separately in sections 4.1 and 4.2, respectively. The FCI distribution is masked for the glaciated regions during  
 337 specific paleoclimate time-slices, as the surface covered under ice-sheets is disconnected from atmospheric  
 338 processes (Grämiger et. al. 2018). In the PLIO results, the regions that experienced Pleistocene glaciation are  
 339 masked with the LGM glacier cover, as the assumption of comparable soil depths in these regions is heavily  
 340 violated. Since spatial and temporal variations in frost cracking do not vary much between the three approaches,  
 341 for brevity we focus our presentation of results on the most recent (Model 3 - Andersen et al., 2015) approach.  
 342 The results of simpler approaches (Model 1, 2; Anderson 1998 and Hales and Roering, 2007) are presented in the  
 343 supplementary material.

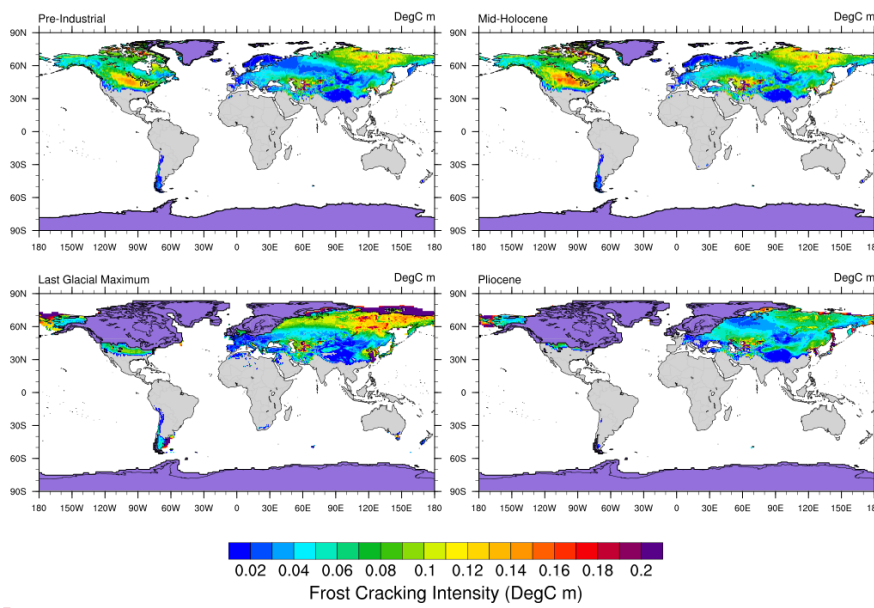
##### 344 4.1. Model 3 - Scenario 1: FCI as a function of thermal gradient and soil thickness (with penalty 345 function)

346 In this scenario, we estimate the global FCI distribution using Model 3 (Andersen et al., 2015) with the penalty  
 347 function, which makes FCI dependent on the distance to water. The predicted global sum of FCI is greatest for  
 348 the MH ( $\sim 31.3997^{\circ}\text{C m}$ ), followed by the PI ( $\sim 30.3235^{\circ}\text{C m}$ ), LGM ( $\sim 23.8277^{\circ}\text{C m}$ ) and PLIO ( $\sim 21.6529^{\circ}\text{C}$   
 349 m). The correlation between FCI values and  $T_{\text{a}}$  is high (Pearson  $r$ : between 0.8 and 0.89) and statistically  
 350 significant (using the 95% level as a threshold to determine significance). On the other hand, the correlation

Formatted: English (US)  
 Field Code Changed  
 Formatted: English (US)  
 Formatted: English (US)  
 Formatted: English (US)  
 Formatted: English (US)  
 Formatted: English (US)  
 Formatted: English (US)  
 Formatted: English (US)  
 Deleted: 4. ¶  
 3.3. Calculation of permafrost extent ¶  
 The permafrost extent in the LGM and present-day simulations were estimated using the approach of Levasseur et al. (2011), where permafrost is assumed to be solely dependent on near surface temperatures, except in high mountainous regions with varied soil types and snow cover. The boundary conditions were adopted from (Renssen and Vandenberghe, 2003), which state that continuous permafrost exists in regions with mean annual near surface temperatures of  $-8^{\circ}\text{C}$  or below, and coldest month temperatures of  $-20^{\circ}\text{C}$  or lower. Furthermore, we also consider the same study's statement that discontinuous permafrost exists in the regions with MAT in the range between  $-8^{\circ}\text{C}$  and  $-4^{\circ}\text{C}$ . ¶  
 Results  
 Deleted: in  
 Deleted: , and present the  
 Deleted: the other two

371 between FCI and MATs is good in the LGM (Pearson r: -0.68), moderate in the PI and MH (Pearson r: -0.3 --  
 372 0.4), and poor in the PLIO (Pearson r: -0.04).

373 For all paleoclimate time slice experiments, the FCI predicted by Model 3 is in the range of 0 – 0.22 °C m at  
 374 higher latitudes (30 °N – 80 °N and 45 °S – 60 °S) (Fig. 6). The maximum FCI values are observed in the higher  
 375 latitudes (50 °N – 80 °N) and show the same pattern as variations in Ta when Ta exceeds 30°C. In the PI and MH  
 376 simulations, the highest FCI is observed in North America (40°N – 55°N and 70°N – 80°N) and Eurasia (35 °N –  
 377 50 °N, 55 °E – 80 °E and 55 °N – 80 °N, 80 °E – 180 °E), with values ranging from -0.08 °C m to -0.2 °C m.  
 378 Low FCI can be observed in South America, with values between 0.02 °C m and 0.05 °C m. This is consistent  
 379 with results from models 1 and 2 (see supplement). In the LGM simulation, the highest FCI values are observed  
 380 in Alaska, Turkmenistan, Uzbekistan, Eastern China and north-eastern latitudes in Eurasia (70 °N – 80 °N, 105  
 381 °E – 180 °E) with values ranging from -0.08 °C m to -0.2 °C m. In the Andes of South America, the frost cracking  
 382 activity is restricted to the geographical range of 12 °S – 55 °S. The highest South American FCI values (~ 0.15  
 383 °C m to ~ 0.22 °C m) are predicted for the southern part of the continent (40 °S – 50 °S).



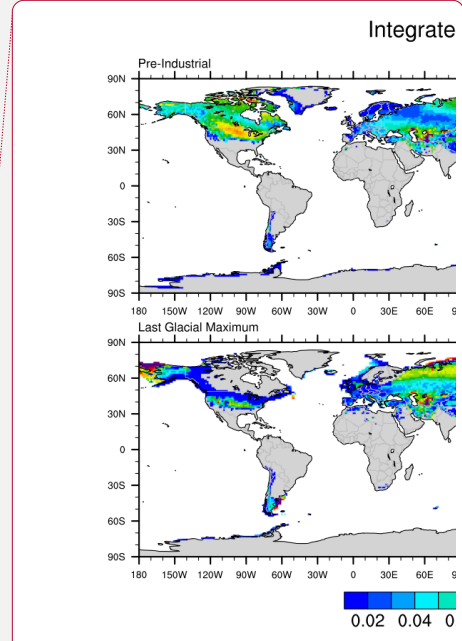
384 **Figure 6. Model 3 (Scenario 1) predicted integrated FCI as a function of thermal gradient and sediment thickness (with**  
 385 **the penalty function) for Pre-Industrial (top-left), Mid-Holocene (top-right), Last Glacial Maximum (bottom-left), and**  
 386 **mid-Pliocene (bottom-right) times (unit: °C m). The grey areas in plots indicates the absence of frost cracking. For all**  
 387 **time slices, the regions covered by ice were removed from the calculation and are highlighted in violet color**  
 388 **(Bracannot et al., 2012). For the PLIO results, the LGM ice cover is used, since the assumption of modern**  
 389 **soil depth is heavily violated in these regions.**

391 In the mid-Pliocene, the maximum FCI values are predicted in the higher latitudes i.e., Alaska (-0.15 °C m - -0.22  
 392 °C m). Moderately high values are predicted for the northern latitudes of Eurasia (0.05 °C m – 0.16 °C m). Overall,

Deleted: 4  
 Deleted: 20  
 Deleted: 80  
 Deleted: 1

Deleted: 1  
 Deleted: 22

Deleted: New Zealand and the western periphery of Antarctica exhibit some frost cracking activity in the LGM driven models.



Deleted: F1 ... [1]

Deleted: Data plotted in this figure are available in the supplemental material for readers interested in plotting / using it for other purposes.

Deleted: For the Last Glacial Maximum time slice and Greenland and Antarctica (all time slices) the regions covered by ice were removed from the calculation and are

Deleted: of Canada and

Deleted: (

Deleted: Greenland (0.02 °C m – 0.12 °C m) and

424 the magnitude of mid-Pliocene FCI is lower than that of all other investigated time slices. The only exceptions are  
425 some high-latitude regions (e.g. Alaska) that exhibit locally higher FCI values in the mid-Pliocene relative to the  
426 PI. Negligible frost cracking is predicted for South America, which is consistent with the results of Model 1  
427 (Anderson, 1998).  
428 For all the time-slices, regions with positive MATs (0 °C to 15 °C) exhibit higher values of FCI where the sediment  
429 cover is thinner (e.g. Middle East Asia). In contrast, predictions of FCI in regions with negative MATs (-5 °C to  
430 -20 °C) and high Ta (30 °C to 40 °C) tend to be higher where sediment cover is thicker (e.g. North East Eurasia).

Deleted: exception

Deleted: NE Canada, eastern Antarctica

Deleted: Less

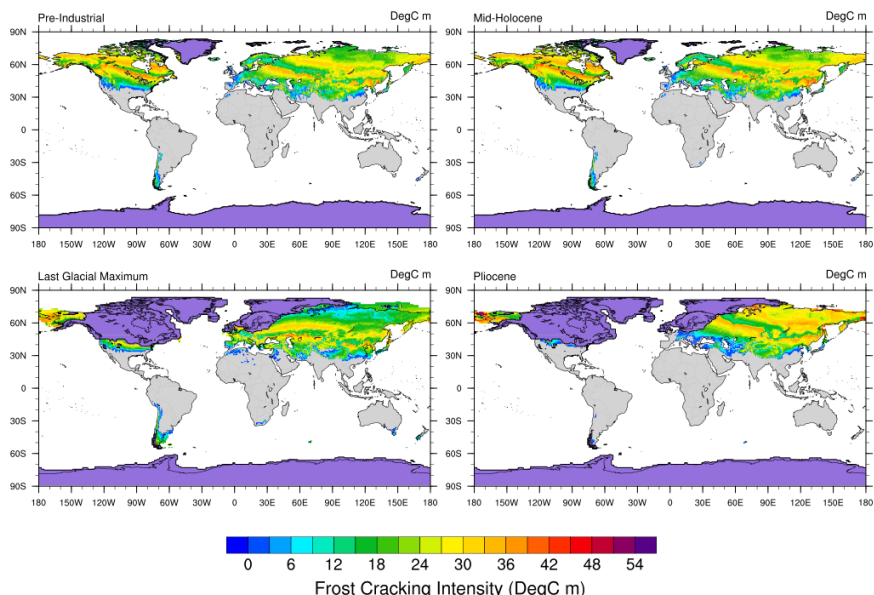
Deleted: activity

431 **4.2. Model 3 - Scenario 2: FCI as a function of thermal gradient and soil thickness (without penalty**  
432 **function)**

433 In this scenario, we estimate global FCI distribution using Model 3 (Andersen et al., 2015) without applying the  
434 penalty function (Fig. 7). The highest magnitude of frost cracking intensity is simulated for the PLIO (~53 °C m),  
435 followed by the MH (~47 °C m), PI (~45 °C m), and LGM (~43 °C m). However, the maximum global sum of  
436 FCI is observed in the MH (~31,3997 °C m), followed by the PI (~30,3235 °C m), LGM (~23,8277 °C m) and  
437 PLIO (~21,6529 °C m) simulations. Similar to the observations in Model 2 (see Supplement S.2), the FCI  
438 distribution is negatively correlated with MATs (Pearson r: between -0.4 and -0.5) and Ta (Pearson r: between  
439 0.9 and 0.95). These correlations are significant (using the 95% threshold to determine significance).

440 In the PI simulations, the maximum FCI values are predicted for the mid-high latitudes (i.e., FCI: 21 – 44 °C m  
441 in 40 °N – 70 °N) of North America and Eurasia. Low to moderate frost cracking is predicted for South America  
442 (i.e., FCI: 6 – 18 °C m in 20 °S – 55 °S). The MH simulations predict a similar FCI pattern and FCI values that  
443 are slightly higher than in the PI (e.g., FCI: 21 – 47 °C m in 40 °N – 70 °N).

444 In the LGM simulation, major portions of North America and Europe are covered by ice-sheets and thus excluded  
445 from our frost cracking models. The simulations yield maximum FCI values for Alaska (i.e. 21 – 44 °C m) and  
446 the mid-high latitudes in Asia (i.e. FCI: 14 – 42 °C m in 35 °N – 65 °N), moderate FCI values in the peri-glacial  
447 regions in North America (i.e. FCI: 18 – 33 °C m in 35 °N – 42 °N), and low FCI values in South America (i.e.  
448 FCI: 4 – 18 °C m in 15 °S – 55 °S). In the PLIO simulation, major frost cracking activity is predicted for Alaska  
449 (i.e. 21 – 48 °C m) and the northern latitudes of Asia (i.e. FCI: 18 – 48 °C m in 30 °N – 80 °N). We do not observe  
450 any significant frost cracking in Europe, North America and South America in the PLIO simulations.



455  
 456 **Figure 7. Model 3 (Scenario 2) predicted integrated FCI as a function of thermal gradient and sediment thickness**  
 457 **(without the penalty function) for Pre-Industrial (top-left), Mid-Holocene (top-right), Last Glacial Maximum (bottom-**  
 458 **left), and mid-Pliocene (bottom-right) times (unit: °C m). The grey areas in plots indicates the absence of frost cracking.**  
 459 **For all time slices, the regions covered by ice were removed from the calculation and are highlighted in**  
 460 **violet color (Bracannot et al., 2012). For the PLIO results, the LGM ice cover is used, since the assumption**  
 461 **of modern soil depth is heavily violated in these regions.**

462 **5. Discussion**

463 In this section, we synthesize and interpret the **global** results of all the models, including scenarios with and  
 464 without the penalty function in Model 3. For brevity, we limit our discussion of regional variations to Tibet,  
 465 Europe and South America. For other regional areas of interest to readers, the data used in the following figures  
 466 is available for download (see acknowledgements). Our presentation of selected regional areas is followed by the  
 467 comparison of modeled FCI with published field observations. We also compare the model outcomes of all the  
 468 three models used in the study. Finally, we discuss the study's limitations.

469 **5.1. Synthesis and Interpretation**

470 This section comprises the synthesis and interpretation of the **global** trends in FCI values predicted by Models 1-  
 471 3 for the investigated paleoclimate simulations (PI, MH, LGM and PLIO). In all the paleoclimate simulations,  
 472 high values of FCI in northern latitudes (60°N – 80°N) in Eurasia and North America coincide with lower MATs  
 473 in the range of -25 °C to -5 °C and very high Ta's in the range of 30 °C to 40 °C. FCI in areas with negative MATs  
 474 is mainly controlled by the Ta values, as higher Ta and high thermal gradients are predicted in the subsurface and

**Deleted:** (from  
**Deleted:** ) at both a global and regional scales.  
**Deleted:** include  
**Deleted:** and permafrost extent in the LGM and present day.  
**Deleted:** the PI and MH  
**Deleted:** 1  
**Deleted:** Furthermore, the soil thickness in some of these areas is as low as 10 – 20 cm in North America, and 40 – 50 cm in Eurasia. The higher values of FCI coincide with positive MATs (~10 °C – 20 °C) in the mid-high latitudes in North America, where Ta values are also high (25 °C – 30 °C) and soil cover thickness is in the range of 50 cm – 60 cm. However, the highest FCI was predicted in the Middle East, which experiences similar MATs and Ta values and has significantly thinner soil cover (0 cm – 20 cm). This indicates that frost cracking is more prevalent in areas with positive MATs and thin or no soil cover. This confirms the findings of (Hales and Roering, 2007, 2009), and Anderson et al. ((2013), 2015)(2015)).  
**Deleted:** and thicker soil cover (~ 80 cm – 100 cm)  
**Deleted:** due to

497 facilitate ice segregation growth (Hales and Roering, 2007; Hallet et al., 1991; Murton et al., 2006; Walder and  
 498 Hallet, 1985).  
 499 We also calculated the global sum of FCI for all paleoclimate time-slices to determine which Cenozoic timescale  
 500 is most important for frost cracking in each model. Furthermore, we compare the global sum of FCI in MH, LGM  
 501 and PLIO to that of PI simulations. Model 1 predicts a maximum FCI for the PI. These are 3.8%, 27%, and 25%  
 502 higher than the FCI values in the MH, LGM, and PLIO simulations, respectively. In Model 2, MH experiences  
 503 maximum FCI, which is 2.4% higher than in the PI, while FCIs in the LGM and PLIO simulations are 15% and  
 504 31% lower than in the PI. In Model 3 (scenario 1), the LGM and MH experience FCI values that are 22% and  
 505 12% higher than in the PI, while FCI in the PLIO is 30% lower than in the PI simulation. In Model 3 (scenario 2),  
 506 the MH experiences the maximum FCI, which is 3.5% higher than in the PI, while FCIs in LGM and PLIO  
 507 simulations are 21% and 29% lower than in the PI. The global sum of FCI estimates are consistent between Model  
 508 1, 2, and 3 (scenario 2) and suggest that maximum frost cracking (weathering) occurred during inter-glacial  
 509 periods (i.e. MH and PI), while the glacial period (LGM) experienced comparatively less frost cracking. The  
 510 above predictions for frost cracking (e.g. in Model 1, 2 and 3 (scenario 2)) are inconsistent with studies of global  
 511 weathering fluxes during glacial and inter-glacial periods, which reported an increase of weathering of ~20% in  
 512 the LGM (compared to the present) (Gibbs and Kump, 1994; Ludwig et al., 1999). This pattern is, however,  
 513 predicted by Model 3 (scenario 1) where the maximum in global frost cracking is predicted for the glacial period  
 514 (LGM). More specifically, Model 3 (scenario 1) predicts an FCI increase of 22% from PI values. This observation  
 515 is also consistent with the findings of a similar work by Marshall et al. (2015), who suggested that frost weathering  
 516 was higher during the LGM than today in unglaciated regions. These results highlight the importance of the  
 517 penalty function (i.e. dependency of FCI on distance to water) in first order (global) estimations of FCI.

Deleted: , both of which

Deleted: A similar effect of temperature and soil thickness on frost cracking intensity is observed in the LGM and PLIO simulations.

## 518 5.2. Influence of past climate on FCI on a global scale

Deleted: at

519 We have investigated the influence of climate change on frost cracking on different spatial scales and through  
 520 geologic time using 3 different frost cracking models (Anderson, 1998; Hales and Roering 2007; Andersen et al.,  
 521 2015) and paleoclimate GCM simulations (Mutz et al., 2018). Our results for Model 3 are presented as maps  
 522 showing time-slice specific FCI anomalies relative to the PI climate simulation on a global scale (Fig. 8a, 9a, 10a),  
 523 in Europe (Fig. 8b, 9b, 10b), Tibet (Fig. 8c, 9c, 10c) and South America (Fig. 8d, 9d, 10d). Furthermore, we  
 524 highlighted where continental ice was located for all time-slices (PI, MH, LGM) or where Pleistocene ice cover  
 525 could result in a violation of our assumption of modern soil thickness (PLIO) (Fig. 8-10). This was done to prevent  
 526 unmerited regional comparisons of simulated FCI.

Deleted: 7

Deleted: Tibet (Fig. 8),

Deleted: 9

Deleted: 10

Deleted: the spatial distribution of FCI in various climates has been compared with the glacier mask (Supplement Fig. 3)

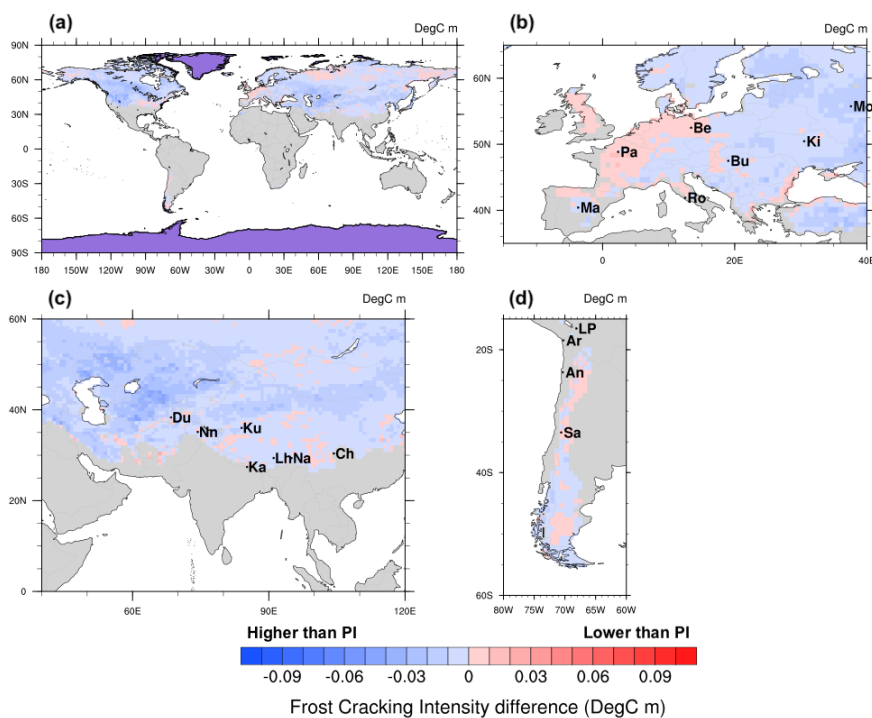
Deleted: and

Deleted: understand the reasons behind the trend of FCI over time

### 527 5.2.1. Differences in FCI between PI and MH climate simulations

528 The differences in FCI between the PI and MH climate simulations are in the range of  $-0.04$  °C m to  $0.02$  °C m  
 529 on a global scale (Fig. 8a). The MH simulation yields higher FCI values for most regions except for parts of  
 530 northern Asia, mid-western Europe, mid North America, the Andes Mountains and parts of Alaska and Tibet.  
 531 These differences may be attributed to the slight changes in MATs in these regions. The PI – MH comparisons  
 532 for Europe (Fig. 8b) reveal very small deviations in MH-FCI from PI conditions ( $\Delta$ FCI  $\approx$   $-0.02$  °C m to  $0.02$  °C  
 533 m). These changes are negative in Western Europe (including areas near the cities of Paris, Berlin and Rome),  
 534 and positive in Eastern Europe (including Budapest, Kiev and Moscow). Tibet exhibits only small ( $-0.02$  °C m),

549 predominantly positive MH-FCI deviations from PI conditions (Fig. 8c). The magnitude of PI-MH FCI differences  
 550 in southwestern South America (Fig. 8d) is similar to that in other regions ( $\Delta FCI \approx -0.02 \text{ }^\circ\text{C m}$  to  $0.02 \text{ }^\circ\text{C m}$ ).



551 Figure 8. Differences between (Model 3) predictions of Pre-Industrial and Mid-Holocene long-term FCI means (unit:  
 552  $^\circ\text{C m}$ ) for (a) the entire Earth surface, (b) Europe, (c) South Asia, and (d) South America. Glacial cover is highlighted  
 553 in violet. City abbreviations: Tibet:- Du – Dushambe, Nm – Srinagar, Ku – Xinjiang, Ka – Kathmandu, Lh – Lhasa,  
 554 Na – Namcha Barwa, Ch – Chenshangou; Europe:- Pa – Paris, Be – Berlin, Mo – Moscow, Ki – Kiev, Ro – Rome, Bu  
 555 – Budapest, Ma – Madrid; South America:- LP – La Paz, Ar – Arica, An – Antofagasta, Sa – Santiago. The regions  
 556 covered by ice were removed from the calculation and are highlighted in violet color (Bracannot et al., 2012).

558 5.2.2. Differences in FCI between PI and LGM climate simulations

559 The differences in FCI between PI and LGM on global scale (Fig. 9a) are highest in the mid-high latitudes ( $\sim 42$   
 560  $^\circ\text{N}$ ) in North America ( $\Delta FCI \approx 0.08 \text{ }^\circ\text{C m}$ ) and northern Asia ( $\sim 75 \text{ }^\circ\text{N}$ ) ( $\Delta FCI \approx 0.07 \text{ }^\circ\text{C m}$ ). The close proximity  
 561 of these regions to the glacier cover in the LGM highlights the possibility of the presence of periglacial  
 562 environments that support frost cracking (Marshall et al., 2015) during the PI. This is also observed in the mid-  
 563 high latitudes in Asia ( $30 \text{ }^\circ\text{N} - 50 \text{ }^\circ\text{N}$ ) ( $\Delta FCI \approx 0.04 \text{ }^\circ\text{C m}$ ), which may be attributed to the positive MATs in this  
 564 region during the PI simulation.

Moved (insertion) [1]

Moved (insertion) [2]

Moved down [3]: Tibet

Moved up [1]: Figure 8.

Moved down [4]: Tibet exhibits only small ( $\sim 0.02 \text{ }^\circ\text{C m}$ ), predominantly positive MH-FCI deviations from PI conditions (Fig.

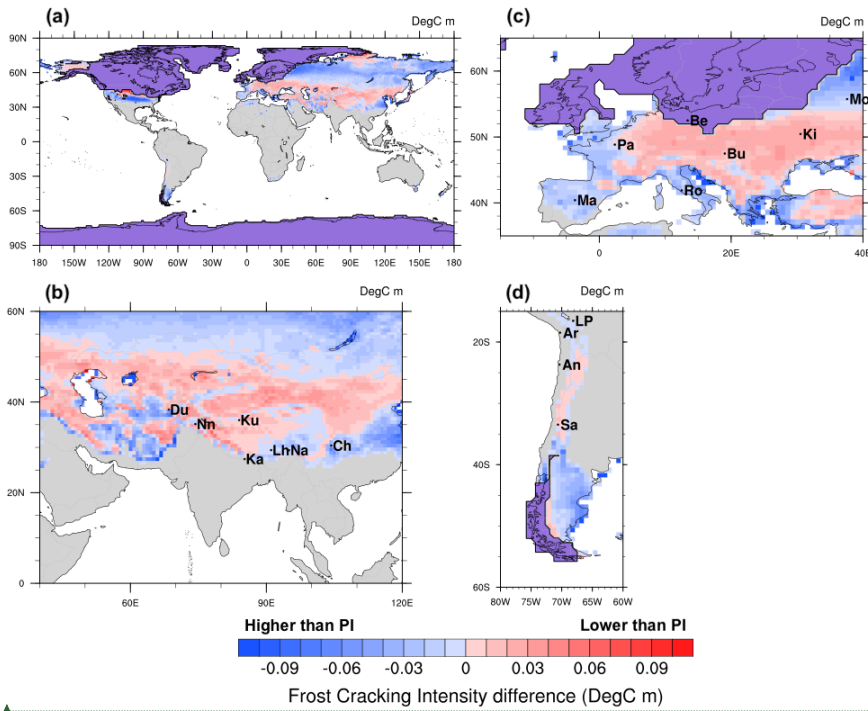
**Deleted:** The differences in FCI between the PI and MH climate simulations are the range of  $-0.04 \text{ }^\circ\text{C m}$  to  $0.02 \text{ }^\circ\text{C m}$ . The MH simulation yields s higher FCI values for most regions except for parts of northern Asia, mid-western Europe, mid North America, Alaska, the Andes Mountains and Tibet. These differences may be attributed to the slight changes in MATs in these regions.

The differences between PI and LGM FCI values are highest in the high latitudes (Fig. 7) in North America ( $\Delta FCI \approx 0.16 \text{ }^\circ\text{C m}$ ) and northern Europe ( $\Delta FCI \approx 0.04 \text{ }^\circ\text{C m}$ ). This is likely due to continental glaciation in these areas (Supplement Fig. 3) leading to low or no frost cracking during LGM. In the mid-high latitudes ( $\sim 50 \text{ }^\circ\text{N}$  to  $70 \text{ }^\circ\text{N}$ ) of Northern Asia, LGM FCI values are higher than in PI FCI values ( $\Delta FCI \approx -0.06 \text{ }^\circ\text{C m}$ ). This can be attributed to an absence of glacial cover and higher Ta values (Fig. 3) in this region during the LGM. However, the LGM FCI values are higher than in the PI simulation ( $\Delta FCI \approx 0.04 \text{ }^\circ\text{C m}$ ) in the mid-high latitudes in Asia ( $30 \text{ }^\circ\text{N} - 50 \text{ }^\circ\text{N}$ ), which may be attributed to the positive MATs in this area during the PI simulation.

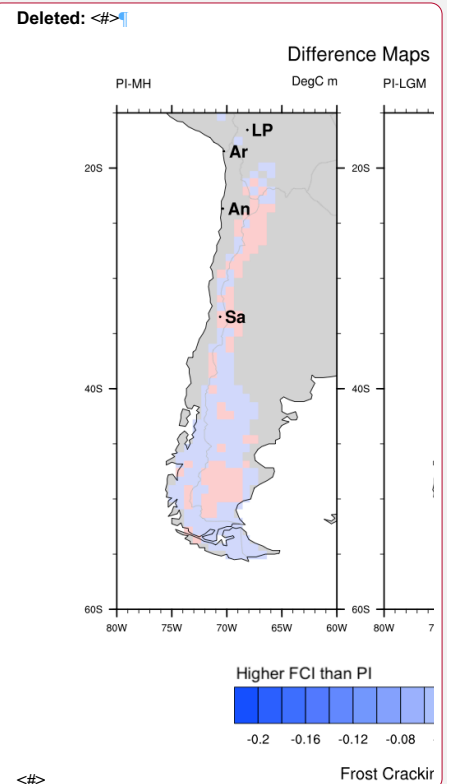
... [2]

Moved down [5]: Europe

Moved (insertion) [4]



Moved up [2]: South America



<#>

Deleted: <#>10

Deleted: <#>in

Deleted: <#>mean

Deleted: <#>(Model 3) between

Moved (insertion) [3]

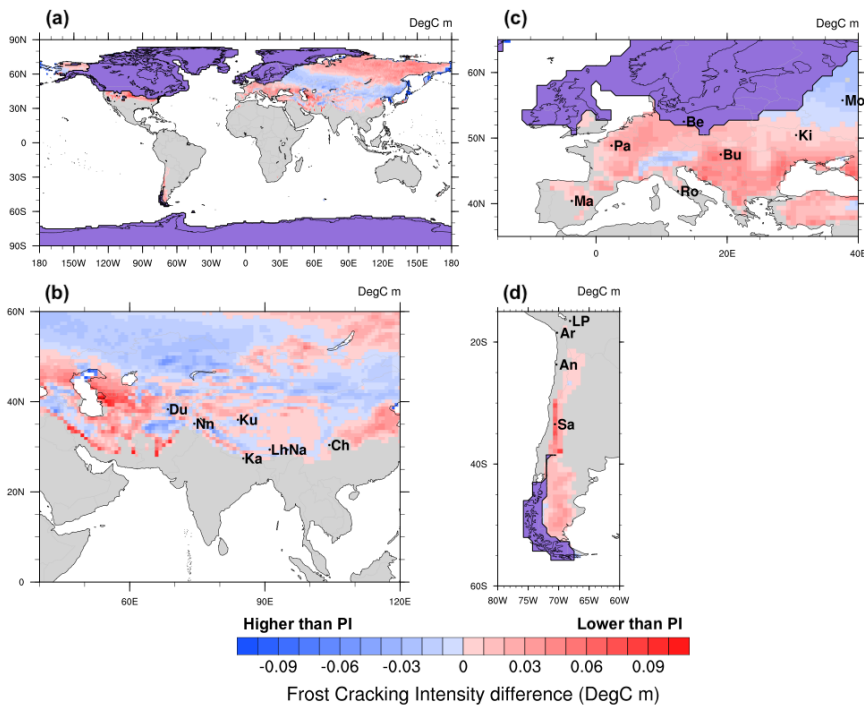
Deleted: <#>Pre-Industrial minus (-) the Mid-Holocene (top-left), Pre-Industrial - Last Glacial Maximum (top-right), and Pre-Industrial - mid-Pliocene (bottom) (unit: °C m) in southwestern South America. City abbreviations:

Moved (insertion) [5]

639 **Figure 9. Differences between (Model 3) predictions of Pre-Industrial and Last Glacial Maximum long-term FCI means**  
 640 **(unit: °C m) for (a) the entire Earth surface, (b) Europe, (c) South Asia, and (d) South America. Glacial cover is**  
 641 **highlighted in violet. City abbreviations: Tibet: Du – Dushambe, Nn – Srinagar, Ku – Xinjiang, Ka – Kathmandu,**  
 642 **Lh – Lhasa, Na – Namcha Barwa, Ch – Chenshangou; Europe: Pa – Paris, Be – Berlin, Mo – Moscow, Ki – Kiev, Ro**  
 643 **– Rome, Bu – Budapest, Ma – Madrid; South America: LP – La Paz, Ar – Arica, An – Antofagasta, Sa – Santiago.**  
 644 **The regions covered by ice were removed from the calculation and are highlighted in violet color (Bracannot et al.,**  
 645 **2012).**

647 However, in the higher latitudes of Asia (~ 50 °N to 70 °N) and South America (~ 40 °S to 50 °S), the LGM  
 648 experiences more frost cracking than the PI ( $\Delta FCI \approx -0.03$  -  $-0.06$  °C m). This can be attributed to higher  $T_a$   
 649 values (Fig. 3) in these regions during the LGM. In central Europe (Fig. 9b), including Paris, Budapest and Kiev,  
 650 the PI shows higher FCI ( $\Delta FCI \approx 0.02$  -  $0.06$  °C m) than the LGM. On the other hand, the LGM simulations  
 651 predict higher FCI ( $\Delta FCI \approx -0.02$  -  $-0.06$  °C m) in southern Europe (including Madrid and Rome). Overall, the  
 652 Tibetan Plateau experiences higher FCI values ( $\Delta FCI \approx 0.06$  °C m) during the PI (Fig. 9c). Only in the eastern  
 653 part of Tibet, near Lhasa, LGM FCI values are higher ( $\Delta FCI \approx 0.04$  °C m). In South America (Fig. 9d), the LGM  
 654 yields lower FCI values ( $\Delta FCI \leq 0.06$  °C m) in the Andes Mountains, and the PI simulation yields lower FCI  
 655 values ( $\Delta FCI > -0.06$  °C m) in the east of the Andes Mountains in the southern part of the region (40 °S – 50 °S).

### 656 5.2.3. Differences in FCI between PI and PLIO climate simulations



669  
 670 **Figure 10. Differences between (Model 3) predictions of Pre-Industrial and Pliocene long-term FCI means (unit: °C m)**  
 671 **for (a) the entire Earth surface, (b) Europe, (c) South Asia, and (d) South America. Maximum Pleistocene glacial cover**  
 672 **is highlighted in violet. City abbreviations: Tibet:- Du – Dushambe, Nn – Srinagar, Ku – Xinjiang, Ka – Kathmandu,**  
 673 **Lh – Lhasa, Na – Namcha Barwa, Ch – Chenshangou; Europe:- Pa – Paris, Be – Berlin, Mo – Moscow, Ki – Kiev, Ro**  
 674 **– Rome, Bu – Budapest, Ma – Madrid; South America:- LP – La Paz, Ar – Arica, An – Antofagasta, Sa – Santiago.**  
 675 **The regions covered by ice were removed from the calculation and are highlighted in violet color (Bracannot et al.,**  
 676 **2012).**

677 Frost cracking is higher in the PI than in the PLIO (Fig. 10a) ( $\Delta FCI \approx 0.04 - 0.08 \text{ } ^\circ\text{C m}$ ) in the mid-to-high  
 678 latitudes of Europe and North America ( $35^\circ\text{N} - 55^\circ\text{N}$ ), and in higher latitudes in Asia ( $50^\circ\text{N} - 80^\circ\text{N}$ ). This can  
 679 be attributed to the warmer climate during PLIO and high  $T_a$  (Fig. 3) in the PI simulation. However, the PLIO  
 680 exhibits marginally higher frost cracking in some regions of Asia and Alaska, where MATs are in the range of  $0$   
 681  $-5 \text{ } ^\circ\text{C}$ .

682 In central to southern Europe, including Madrid, Paris, Rome, Budapest and Kiev, PI-FCI values are moderate  
 683 ( $\Delta FCI \approx 0.02 \text{ } ^\circ\text{C m} - 0.06 \text{ } ^\circ\text{C m}$ ). On the Tibetan Plateau (Fig. 10c), PI-FCI values are higher ( $\Delta FCI \approx 0.04 \text{ } ^\circ\text{C m}$ )  
 684 over most of the region, except for the eastern slopes of Himalayas, where PLIO-FCI values are higher than  
 685 European region ( $\Delta FCI \approx -0.04 \text{ } ^\circ\text{C m}$ ). South America experienced largest differences in FCI ( $\Delta FCI \approx 0.02 \text{ } ^\circ\text{C m}$   
 686 to  $0.08 \text{ } ^\circ\text{C m}$ ) (Fig. 10d). This is likely caused by high temperatures in the Pliocene (Mutz et al., 2018), which  
 687 prevented the bedrock in the mid-latitude regions of South America to reach the FCW.

688 In summary, the comparison of differences between paleo-FCI and PI-FCI indicate a low impact of changing



689 surface temperatures between the PI and MH simulations on frost cracking. This is not surprising given the  
690 relatively small climatological differences between the simulations. The differences in FCI between the PLIO and  
691 PI are more varied, but generally greater. The LGM simulation produced the greatest differences in FCI with  
692 respect to the PI simulation. These differences can be attributed to increased glaciation and a much colder climate  
693 in higher latitudes, including North America and Europe. High LGM-FCI values were exhibited east of the Andes  
694 Mountains in the southern part of South America, possibly due to lower MATs (Fig. 2) and high Ta values (~ 20  
695 °C – 25 °C) (Fig. 3) during the LGM. The above interpretations are in agreement with Mutz et al. (2018) and  
696 Mutz and Ehlers (2019) who suggested minor deviation of MH MATs from PI values for these regions, and higher  
697 deviations in the LGM and PLIO simulations.

### 698 5.3. Comparison to previous related studies

699 In this section, we discuss the broad trends of modeled FCI in the context of variations in MAT, Ta, and water  
700 availability. We do this to document how these changes compare to findings of previous studies. We found that  
701 FCI and Ta are highly (and significantly) correlated in our models. For example, Model 3 (scenario 1) results  
702 yield significant Pearson r values in the range of 0.8 – 0.9. This is consistent with findings by Rempel et al. (2016),  
703 who suggested that for the same MAT and rock properties, FCI is expected to be higher for regions with higher  
704 Ta, as steeper temperature gradients supports more liquid transport. Walder and Hallet (1985) suggested that FCI  
705 is higher for moderately low, negative MATs and that frost cracking in cold regions could persist due to water  
706 transport in cold bedrock. The assumption of positive temperatures (and availability of liquid water) at either  
707 boundary (i.e. at surface and 20 m depth) in Models 1, 2 and 3 is inconsistent with above statement. The inclusion  
708 of a penalty function, which represents the dependency of FCI on distance to water, leads to higher global sums  
709 of FCI during colder climates. More specifically, the inclusion of the penalty function predicts LGM-FCI values  
710 to be 20% higher than in the PI. This is in line with studies of global chemical weathering fluxes (Gibbs and  
711 Kump, 1994; Ludwig et al., 1999). Finally, recent work (Marshall et al., 2015a, 2017) for Western Oregon, USA,  
712 suggested that periglacial processes were vigorous during the LGM, which is supported by our model showing  
713 increased FCI values in the LGM (see Fig. 9a) for periglacial regions (42 °N – 44 °N; 115 °W – 125 °W) in North  
714 America. Taken together, previous studies are consistent with the broad trends in FCI predicted by our global  
715 analysis.

### 716 5.4. Inter-comparison of Models 1-3

717 A comparison of the FCI predicted by the three models for the different time slices highlights some key differences  
718 (Fig. 6, and supplement Figs. 1, 2). The pattern of global sums in FCI values in specific time-slices is different in  
719 all the three models, which can be accredited to different inputs considered in each model. These inputs include,  
720 the availability of water for frost cracking by segregation ice growth, and the volume of available water (with and  
721 without consideration of distance to water). For example, Model 1, Model 2, Model 3 (scenario 1: with penalty  
722 function), and Model 3 (scenario 2: without penalty function) predict the global sum of FCI to be greatest in the  
723 PI, MH, LGM and MH, respectively.

724 Model 1 predicts the maximum FCI values in the regions with MATs in the range of -10 °C to -5 °C, relatively  
725 low FCI values in regions with MATs of -5 °C – 0 °C, and very low values in regions characterized by high MATs  
726 above 0 °C. In contrast, Model 2 (Supplement Fig. 2) and Model 3 yield maximum FCI values for positive MATs  
727 with high Ta, as observed in previous studies (Andersen et al., 2015; Anderson et al., 2013; Hales and Roering,

**Deleted:** In a previous study by Amitrano et al. (2012), evidence of frost cracking in the Swiss Alps was investigated in high-alpine rock walls. The maximum values for FCI were observed in the temperature range of 0 °C to -5 °C for granite and gneiss lithologies. The measurement site was a south facing cliff at an elevation of about ~3500 m a.s.l. with local mean annual air temperature of -7.3 °C (1961 - 1990) and mean annual rock temperature of -2 °C to 3 °C (Hasler et al., 2011). Amitrano et al., (2012) suggested that increased frost cracking for warmer periods could be interpreted as an effect of thermal dilation of cracks. This is supported by our study, as in Model 3 results, the northern latitudes in Eurasia and mid latitudes in North America and Alaska show high values of frost cracking intensity (~ 0.08 °C m – 0.18 °C m) in PI, MH and PLIO simulations. Another study (Girard et al., 2013) in the Swiss Alps (Jungfrauoch) applied acoustic emission techniques and suggests increased FCI for subsurface temperatures ranging from 0 °C to -15 °C. Furthermore, Girard et al. (2013) suggested that sustained freezing can yield much stronger frost cracking activity than repeated freeze-thaw cycling. Larger rates of acoustic energy detected at negative temperatures (T < 0 °C) suggest that water migration and segregation ice growth play and important role in frost cracking. This supports our Model 3 results for the LGM simulations in northern Eurasia and Alaska, which show high FCI values in the range of ~ 0.12 °C m – 0.22 °C m. ¶

Hales and Roering (2007) suggested that FCI is higher near the surface, up to a penetration depth of 4 m, because the steepest thermal gradients are near to the surface. In contrast to field studies (Amitrano et al., 2012; Girard et al., 2013), Hales and Roering (2007) suggested that positive MATs account for higher FCI due to the higher availability of water for segregation ice growth, which is consistent with this study's high FCI in the mid-high latitudes of North America (~ 40 °N – 50 °N during PI, MH and PLIO simulations and ~ 35 °N – 45 °N during LGM simulation) and mid-latitudes in South America (~ 15 °S – 55 °S during PI, MH and LGM simulations). ¶

Anderson et al. (2013) suggested that FCI is higher for moderately low, negative MATs and that frost cracking in cold regions could persist due to water transport in cold bedrock. Furthermore, Andersen et al. (2015) suggested that frost cracking can be active in moderately warm climates provided that sediment cover is very thin (< 10 cm) and the surface temperature is occasionally lowered into the frost cracking window. The above findings are in agreement with our computed FCI (~ 0.16 °C m – 0.2 °C m) in the middle east (~ 36 °N – 48 °N and 54 °E – 80 °E), which has a relatively thin sediment cover (> 5 cm) and MAT range of 5 °C to 15 °C. Finally, recent work (Marshall et al., 2015, 2017) for Western Oregon, USA, suggested that periglacial processes were vigorous during the LGM, which is supported by our model showing maximum FCI values ( 0.12 °C m to 0.3

**Deleted:** spatial extent

**Deleted:** frost cracking

**Deleted:** , namely

**Deleted:** .

**Deleted:** the glaciated region (Supplement Fig. 3) in North America and Greenland exhibits the occurrence of frost cracking in

**Deleted:** significantly reduced frost cracking in

**Deleted:** and the complete absence of frost cracking in

851 2007; Marshall et al., 2015). In Model 3, the soil thickness plays an important role in the estimation of the FCI.  
852 The model predicts high FCI values for areas with low soil thickness, such as < 5 cm in Eurasia (55 °E – 80 °E,  
853 35 °N – 50 °N) and 10 cm to 20 cm for North America (50 °N – 63 °N; 70 °N – 80 °N). This result is in close  
854 agreement with Andersen et al. (2015). Due to the lower penetration depths of the freezing front, the FCI is  
855 considerably dampened in the presence of the soil cover, thereby limiting the bedrock from reaching FCW in  
856 cases of positive MATs (Andersen et al., 2015).  
857 The spatial pattern of frost cracking in Model 3 is influenced by consideration of segregation ice growth, in which  
858 the available volume of water (V<sub>w</sub>) in the vicinity of an ice lens is critical. Segregation ice growth and sediment  
859 cover are responsible for the observed patterns in FCI. The other models considered (see supplement Fig. 1, 2)  
860 do not explicitly account for both these processes and therefore produce different predictions of the FCI in some  
861 regions.

862

### 863 5.5. Model Limitations

864 Here we discuss the limitations of the 3 frost cracking models and uncertainties stemming from the application of  
865 the ECHAM5 simulations as input to these models. One of the most important limitations in this study is the use  
866 of the same soil thickness for each of our paleoclimate time-slices (Wieder, 2014). In reality, the soil thickness  
867 may be different for PI, MH, LGM, and PLIO due to erosion and sedimentation, and temporal variations in soil  
868 production. However, there are currently no other global estimates of paleo soil thickness available. Therefore,  
869 using present-day thickness remains the best-informed and feasible approach. Nevertheless, we stress that our  
870 modelled FCI values should be regarded as the predicted FCI response to climate change without consideration  
871 of weathering – soil thickness dynamics. Furthermore, uniform thermal diffusivity and porosity were used for  
872 bedrock and sediment cover over the globe for simplification, even though thermal diffusivity and porosity vary  
873 for different Earth materials. The application of different thermal diffusivities for individual lithologies was not  
874 considered, although typical thermoconductivity variations of rocks can vary by a factor of 2-3 at the most (Ehlers,  
875 2005). In addition, our models neglect the hydrogeological properties of bedrock, including moisture content and  
876 permeability for the calculation of subsurface temperature variations, which may influence water availability for  
877 frost cracking. To the best of our knowledge, there are no global inventories of these properties that are suited for  
878 studies such as ours. In our approach, we assume that these material properties are spatially and temporally  
879 constant. As a result, our predictions are only suited as adequate representations of regional trends in FCI, and the  
880 reader is advised that local deviations from our values are likely and will depend on near surface geologic and  
881 hydrologic variations. Although the GCM simulations presented are at a high-resolution (from the perspective of  
882 the climate modeling community) they are nevertheless coarse from the perspective of local geomorphic  
883 processes. The coarse spatial resolution of our models raises several issues for more detailed geomorphic analyses.  
884 More specifically, in regions with bare bedrock, the model assumes the presence of a soil layer with 30% porosity,  
885 which compromises our model results. Furthermore, the coarse spatial resolutions of the paleoclimate simulations  
886 (a ~ 80 x 80 km horizontal grid) and low soil thickness spatial resolution (5 km) complicates the consideration of  
887 subgrid variations in regions characterised by complex and high topography (e.g. European Alps, Himalayas or  
888 Andes). For future studies in such terrain, this problem may be addressed by regional climate downscaling (2.g.  
889 Fiddes and Gruber, 2014 and Wang et al., 2021) and the use of high resolution lithologic, and soil distribution

Deleted: produces

Formatted: English (US)

Field Code Changed

Formatted: English (US)

Deleted: greater

892 data (when available). A further source of uncertainties stems from possible inaccuracies in paleoclimate estimates  
893 that drive the frost cracking models. The reader is referred to Mutz et al. (2018) for further discussion of the  
894 GCM's limitations. Given the above limitations, we cautiously highlight that the results presented here are  
895 essentially maps of FCI sensitivity to climate change forcing. Although broad agreement is found between our  
896 predictions and previous work (Section 5.5), we caution that geologic and hydrologic complexities in the 'real  
897 world' may produce variations in FCI driven by hydrologic and geologic heterogeneities we are unable to account  
898 for.  
899 Finally, it is worth noting that only selected time slices were evaluated here. Although the LGM was a significant  
900 global glacial event, previous (and more extreme) ice ages occurred in the Quaternary. Therefore, the spatial  
901 patterns of FCI predicted here may not match observations in all areas, particularly where they have a 'periglacial  
902 hangover' of frost cracking from previous glaciations.

## 903 6. Conclusions

904 We presented three approaches to quantify the frost cracking intensity (FCI) for different times in the Late  
905 Cenozoic, namely pre-industrial (PI, ~1850 CE), Mid-Holocene (MH, ~6 ka), Las Glacial Maximum (LGM, ~21  
906 ka) and mid-Pliocene (PLIO, ~3 Ma). These approaches are based on process-informed frost cracking models and  
907 their coupling to paleoclimate simulations (Mutz et al., 2018). A simple one-dimensional heat conduction model  
908 (Hales and Roering, 2007) was applied along with FCI estimation approaches from Anderson (1998) and  
909 Andersen et al. (2015). Our analysis and presentation of results focused on the most recent and more thoroughly  
910 parameterized approach of Andersen et al., (2015; Model 3). Specifically, we quantified the change in direction  
911 and magnitude of FCI in the above-mentioned climate states with respect to the PI control simulation. The major  
912 findings of our study include:

- 913 1. The latitudinal extent of frost cracking in the PI and MH are very similar, in Eurasia (28 °N – 80 °N),  
914 North America (40 °N – 80 °N) and South America (20 °S – 55 °S). During the LGM, the FCI extent is  
915 reduced in Eurasia (28 °N – 78 °N) and North America (35 °N – 75 °N), and increased in South America  
916 (15 °S – 55 °S). This can be attributed to extensive glaciation in the northern parts of Canada, Greenland  
917 and Northern Europe not favoring the frost cracking process due to more persistently cold conditions in  
918 these regions. In the PLIO, the FCI extent is similar to that of PI in Eurasia (30 °N – 80 °N) and North  
919 America (40 °N – 85 °N). PLIO-FCI values are higher in Canada (~ 0.16 °C m to 0.18 °C m) and  
920 Greenland (~ 0.08 °C m), but significantly reduced in South America (21 °S – 55 °S) with values of FCI  
921 below 0.02 °C m.
- 922 2. MH climatic conditions induce only small deviations of FCI from PI values, whereas the colder (LGM)  
923 and warmer (PLIO) climates produce larger FCI anomalies, which are consistent with the findings of  
924 Mutz and Ehlers, (2019).
- 925 3. Global sums of the FCI predicted by Model 3 - scenario 1, which is based on Andersen et al., (2015)  
926 which makes FCI dependent on distance to water, are highest for the LGM. Our models predict a global  
927 FCI increase of 22% (relative to PI) in non-glaciated regions for this time period.

928 The predicted changes in FCI presented here do not entirely confirm our hypothesis that: Late Cenozoic global  
929 climate change resulted in varying intensity in FCI such that more intense frost cracking occurs at lower latitudes  
930 during colder climates. Of particular interest is that although we document latitudinally influenced spatial and

**Deleted:** Anderson et al. ((2013)(1998)).

**Deleted:** <#>Higher frost cracking intensities in the PI simulation spatially correlate with the occurrence of continuous permafrost in the PD at higher latitudes in Eurasia and North America. On the other hand, during the LGM, high frost cracking in Alaska and northern latitudes of Eurasia show a good correlation with continuous predicted permafrost of the same time.¶

**Formatted:** Space After: 0 pt

939 temporal changes in FCI, these changes are not uniform at the same latitude. The largest changes in FCI between  
940 time slices occur in different geographic regions at different time periods meaning that a more simplified approach  
941 of assuming only latitudinal shifts in FCI between cold and warm periods is not sufficient and that spatial changes  
942 in global climate need to be considered.  
943 Finally, we suggest that Model 3 can be adapted in future work to regional conditions, using field geological and  
944 hydrogeological parameters for better accuracy (Andersen et al., 2015). The results of this study can further be  
945 used in modelling the erosion and denudation processes related to frost cracking, or for the interpretation of  
946 catchment average erosion rates from cosmogenic radionuclide data. Predictions for potential future sites that are  
947 prone to hazards related to frost cracking, such as rockfall, can be generated by coupling these models to climate  
948 simulations forced with different greenhouse gas concentration scenarios representing different possible climate  
949 conditions of the future.

Deleted: <#>taken into account

Field Code Changed

#### 950 Code availability

951 The code and data used in this study are freely available upon request.

#### 952 Author contributions

953 HS, SM and TAE designed the initial model setup and simulation programs and conducted model modifications,  
954 simulation runs and analysis. HS and TAE prepared the manuscript with contributions from SM.

#### 955 Competing interests

956 The authors declare that they have no competing interests.

#### 957 Acknowledgements:

958 H.S, S.G.M. and T.A.E. acknowledge support by Open Access Publishing Fund of University of Tübingen. We  
959 thank two anonymous reviewers for their constructive reviews. The climate model results used in this study are  
960 available via information provided in Mutz et al., (2018). H.S and T.A.E. acknowledge support from the Research  
961 Training Group 1829 Integrated Hydrosystem Modelling, funded by the German Research Foundation (DFG). In  
962 addition, T.A.E, acknowledges support from the German priority research program *EarthShape: Earth Surface*  
963 *Shaping by Biota* (SPP-1803; grant EH329/172), and support from the California Institute of Technology Moore  
964 Distinguished Scholar program. TAE is a member of the Machine Learning Cluster of Excellence, funded by the  
965 German Research Foundation DFG (EXC 2064/1, Project 390727645)

Deleted: XX and YY

Deleted: The primary model results from this study (Model 3) are available in the supplemental material for plotting / use by interested readers.

Deleted: 14

#### 966 References

967 Abe-Ouchi, A., Saito, F., Kageyama, M., Braconnot, P., Harrison, S. P., Lambeck, K., Otto-Bliesner, B. L., Peltier,  
968 W. R., Tarasov, L., Peterschmitt, J.-Y., and Takahashi, K.: Ice-sheet configuration in the CMIP5/PMIP3 Last  
969 Glacial Maximum experiments, *Geosci. Model Dev.*, 8, 3621–3637, <https://doi.org/10.5194/gmd-8-3621-2015>,  
970 2015.

977 Acosta, V. T., Schildgen, T. F., Clarke, B. A., Scherler, D., Bookhagen, B., Wittmann, H., von Blanckenburg, F.,  
978 and Strecker, M. R.: Effect of vegetation cover on millennial-scale landscape denudation rates in East Africa, 7,  
979 408–420, <https://doi.org/10.1130/1402.1>, 2015.

980 Adams, B. A., Whipple, K. X., Forte, A. M., Heimsath, A. M., and Hodges, K. V.: Climate controls on erosion in  
981 tectonically active landscapes, *Sci. Adv.*, 6, eaaz3166, <https://doi.org/10.1126/sciadv.aaz3166>, 2020.

982 Amitrano, D., Gruber, S., and Girard, L.: Evidence of frost-cracking inferred from acoustic emissions in a high-  
983 alpine rock-wall, *Earth and Planetary Science Letters*, 341–344, 86–93,  
984 <https://doi.org/10.1016/j.epsl.2012.06.014>, 2012.

985 Andersen, J. L., Egholm, D. L., Knudsen, M. F., Jansen, J. D., and Nielsen, S. B.: The periglacial engine of  
986 mountain erosion - Part 1: Rates of frost cracking and frost creep, *Earth Surf. Dynam.*, 3, 447–462,  
987 <https://doi.org/10.5194/esurf-3-447-2015>, 2015.

988 Anderson, R. S.: Near-surface Thermal Profiles in Alpine Bedrock: Implications for the Frost Weathering of Rock,  
989 *Arctic and Alpine Research*, 30, 362–372, <https://doi.org/10.1080/00040851.1998.12002911>, 1998.

990 Anderson, R. S., Anderson, S. P., and Tucker, G. E.: Rock damage and regolith transport by frost: an example of  
991 climate modulation of the geomorphology of the critical zone: ROCK DAMAGE AND REGOLITH  
992 TRANSPORT BY FROST, *Earth Surf. Process. Landforms*, 38, 299–316, <https://doi.org/10.1002/esp.3330>, 2013.

993 Arnold, L., Bréon, F.-M., and Brewer, S.: The Earth as an extrasolar planet: the vegetation spectral signature today  
994 and during the last Quaternary climatic extrema, *International Journal of Astrobiology*, 8, 81–94,  
995 <https://doi.org/10.1017/S1473550409004406>, 2009.

996 Bigelow, N. H., Brubaker, L. B., Edwards, M. E., Harrison, S. P., Prentice, I. C., Anderson, P. M., Andreev, A.  
997 A., Bartlein, P. J., Christensen, T. R., Cramer, W., Kaplan, J. O., Lozhkin, A. V., Matveyeva, N. V., Murray, D.  
998 F., McGuire, A. D., Razzhivin, V. Y., Ritchie, J. C., Smith, B., Walker, D. A., Gajewski, K., Wolf, V., Holmqvist,  
999 B. H., Igarashi, Y., Kremenetskii, K., Paus, A., Pisaric, M. F. J., and Volkova, V. S.: Climate change and Arctic  
1000 ecosystems: I. Vegetation changes north of 55°N between the last glacial maximum, mid-Holocene, and present,  
1001 108, <https://doi.org/10.1029/2002JD002558>, 2003.

1002 Botsyun, S., Ehlers, T. A., Mutz, S. G., Methner, K., Krsnik, E., and Mulch, A.: Opportunities and Challenges for  
1003 Paleointensity in “Small” Orogens: Insights From the European Alps, *Geophysical Research Letters*, 47,  
1004 e2019GL086046, <https://doi.org/10.1029/2019GL086046>, 2020.

1005 [Braconnot, P., Harrison, S., Kageyama, M. et al. Evaluation of climate models using palaeoclimatic data. \*Nature\*](#)  
1006 [Clim Change](#) 2, 417–424 (2012). <https://doi.org/10.1038/nclimate1456>

1007 Davidson, G. P. and Nye, J. F.: A photoelastic study of ice pressure in rock cracks, *Cold Regions Science and*  
1008 *Technology*, 11, 141–153, [https://doi.org/10.1016/0165-232X\(85\)90013-8](https://doi.org/10.1016/0165-232X(85)90013-8), 1985.

1009 Delunel, R., van der Beek, P. A., Carcaillet, J., Bourlès, D. L., and Valla, P. G.: Frost-cracking control on  
1010 catchment denudation rates: Insights from in situ produced <sup>10</sup>Be concentrations in stream sediments (Ecrins–

Formatted: English (US)

1011 Pelvoux massif, French Western Alps), *Earth and Planetary Science Letters*, 293, 72–83,  
1012 <https://doi.org/10.1016/j.epsl.2010.02.020>, 2010.

1013 Dietrich, S., Werner, M., Spanghel, T., and Lohmann, G.: Influence of orbital forcing and solar activity on water  
1014 isotopes in precipitation during the mid - and late Holocene, 9, 13–26, <https://doi.org/10.5194/cp-9-13-2013>, 2013.

1015 Dowsett, H., Robinson, M., Haywood, A., Salzmann, U., Hill, D., Sohl, L., Chandler, M., Williams, M., Foley,  
1016 K., and Stoll, D.: The PRISM3D paleoenvironmental reconstruction, *Stratigraphy*, 7, 123–139, 2010.

1017 Draebing, D., Haberkorn, A., Krautblatter, M., Kenner, R., and Phillips, M.: Thermal and Mechanical Responses  
1018 Resulting From Spatial and Temporal Snow Cover Variability in Permafrost Rock Slopes, Steintaelli, Swiss Alps:  
1019 Thermal and Mechanical Responses to Snow in Permafrost Rock Slopes, *Permafrost and Periglac. Process.*, 28,  
1020 140–157, <https://doi.org/10.1002/ppp.1921>, 2017.

1021 Ehlers, T. A. and Poulsen, C. J.: Influence of Andean uplift on climate and paleoaltimetry estimates, *Earth and*  
1022 *Planetary Science Letters*, 281, 238–248, <https://doi.org/10.1016/j.epsl.2009.02.026>, 2009.

1023 Eppelbaum, T. A., Kutasov, I., and Pilchin, A.: Thermal Properties of Rocks and Density of Fluids, in: *Applied*  
1024 *Geothermics*, Springer-Verlag Berlin Heidelberg, 99–149, 2014.

1025 Eppes, M.-C. and Keanini, R.: Mechanical weathering and rock erosion by climate-dependent subcritical cracking:  
1026 WEATHERING BY SUBCRITICAL CRACKING, *Rev. Geophys.*, 55, 470–508,  
1027 <https://doi.org/10.1002/2017RG000557>, 2017.

1028 Etheridge, D. M., Steele, L. P., Langenfelds, R. L., Francey, R. J., Barnola, J.-M., and Morgan, V. I.: Natural and  
1029 anthropogenic changes in atmospheric CO<sub>2</sub> over the last 1000 years from air in Antarctic ice and firn, *Journal of*  
1030 *Geophysical Research: Atmospheres*, 101, 4115–4128, <https://doi.org/10.1029/95JD03410>, 1996.

1031 Etheridge, D. M., Steele, L. P., Francey, R. J., and Langenfelds, R. L.: Atmospheric methane between 1000 A.D.  
1032 and present: Evidence of anthropogenic emissions and climatic variability, *Journal of Geophysical Research:*  
1033 *Atmospheres*, 103, 15979–15993, <https://doi.org/10.1029/98JD00923>, 1998.

1034 Fiddes, J. and Gruber, S.: TopoSCALE v.1.0: downscaling gridded climate data in complex terrain, *Geosci. Model*  
1035 *Dev.*, 7, 387–405, <https://doi.org/10.5194/gmd-7-387-2014>, 2014.

1036 Gibbs, M. T. and Kump, L. R.: Global chemical erosion during the Last Glacial Maximum and the present:  
1037 Sensitivity to changes in lithology and hydrology, *Paleoceanography*, 9, 529–543,  
1038 <https://doi.org/10.1029/94PA01009>, 1994.

1039 Girard, L., Gruber, S., Weber, S., and Beutel, J.: Environmental controls of frost cracking revealed through in situ  
1040 acoustic emission measurements in steep bedrock: IN SITU MEASUREMENTS OF FROST CRACKING,  
1041 *Geophys. Res. Lett.*, 40, 1748–1753, <https://doi.org/10.1002/grl.50384>, 2013.

1042 Hales, T. C. and Roering, J. J.: Climatic controls on frost cracking and implications for the evolution of bedrock  
1043 landscapes, *J. Geophys. Res.*, 112, F02033, <https://doi.org/10.1029/2006JF000616>, 2007.

1044 Hales, T. C. and Roering, J. J.: A frost “buzzsaw” mechanism for erosion of the eastern Southern Alps, New  
1045 Zealand, *Geomorphology*, 107, 241–253, <https://doi.org/10.1016/j.geomorph.2008.12.012>, 2009.

1046 Hallet, B., Walder, J. S., and Stubbs, C. W.: Weathering by segregation ice growth in microcracks at sustained  
1047 subzero temperatures: Verification from an experimental study using acoustic emissions, *Permafrost Periglac.*  
1048 *Process.*, 2, 283–300, <https://doi.org/10.1002/ppp.3430020404>, 1991.

1049 Harrison, S. P., Yu, G., Takahara, H., and Prentice, I. C.: Diversity of temperate plants in east Asia, *Nature*, 413,  
1050 129–130, <https://doi.org/10.1038/35093166>, 2001.

1051 Hasler, A., Gruber, S., and Haerberli, W.: Temperature variability and offset in steep alpine rock and ice faces,  
1052 *The Cryosphere*, 5, 977–988, <https://doi.org/10.5194/tc-5-977-2011>, 2011.

1053 Haywood, A. M., Dowsett, H. J., Otto-Bliesner, B., Chandler, M. A., Dolan, A. M., Hill, D. J., Lunt, D. J.,  
1054 Robinson, M. M., Rosenbloom, N., Salzmann, U., and Sohl, L. E.: Pliocene Model Intercomparison Project  
1055 (PlioMIP): experimental design and boundary conditions (Experiment 1), *Geosci. Model Dev.*, 3, 227–242,  
1056 <https://doi.org/10.5194/gmd-3-227-2010>, 2010.

1057 Herman, F. and Champagnac, J.-D.: Plio-Pleistocene increase of erosion rates in mountain belts in response to  
1058 climate change, *Terra Nova*, 28, 2–10, <https://doi.org/10.1111/ter.12186>, 2016.

1059 Herman, F., Seward, D., Valla, P. G., Carter, A., Kohn, B., Willett, S. D., and Ehlers, T. A.: Worldwide  
1060 acceleration of mountain erosion under a cooling climate, *Nature*, 504, 423–426,  
1061 <https://doi.org/10.1038/nature12877>, 2013.

1062 Kellerer-Pirklbauer, A.: Potential weathering by freeze-thaw action in alpine rocks in the European Alps during a  
1063 nine year monitoring period, *Geomorphology*, 296, 113–131, <https://doi.org/10.1016/j.geomorph.2017.08.020>,  
1064 2017.

1065 Lease, R. O. and Ehlers, T. A.: Incision into the Eastern Andean Plateau During Pliocene Cooling, *Science*, 341,  
1066 774–776, <https://doi.org/10.1126/science.1239132>, 2013.

1067 Lohmann, G., Pfeiffer, M., Laepple, T., Leduc, G., and Kim, J.-H.: A model-data comparison of the Holocene  
1068 global sea surface temperature evolution, 9, 1807–1839, <https://doi.org/10.5194/cp-9-1807-2013>, 2013.

1069 Lorenz, S. J. and Lohmann, G.: Acceleration technique for Milankovitch type forcing in a coupled atmosphere-  
1070 ocean circulation model: method and application for the Holocene, *Climate Dynamics*, 23, 727–743,  
1071 <https://doi.org/10.1007/s00382-004-0469-y>, 2004.

1072 Ludwig, W., Amiotte-Suchet, P., and Probst, J.: Enhanced chemical weathering of rocks during the last glacial  
1073 maximum: a sink for atmospheric CO<sub>2</sub>, *Chemical Geology*, 159, 147–161, [https://doi.org/10.1016/S0009-  
1074 2541\(99\)00038-8](https://doi.org/10.1016/S0009-2541(99)00038-8), 1999.

1075 Marshall, J. A., Roering, J. J., Bartlein, P. J., Gavin, D. G., Granger, D. E., Rempel, A. W., Praskievicz, S. J., and  
1076 Hales, T. C.: Frost for the trees: Did climate increase erosion in unglaciated landscapes during the late  
1077 Pleistocene?, *Sci. Adv.*, 1, e1500715, <https://doi.org/10.1126/sciadv.1500715>, 2015.

1078 Marshall, J. A., Roering, J. J., Gavin, D. G., and Granger, D. E.: Late Quaternary climatic controls on erosion  
1079 rates and geomorphic processes in western Oregon, USA, *Geological Society of America Bulletin*, 129, 715–731,  
1080 <https://doi.org/10.1130/B31509.1>, 2017.

1081 Matsuoka, N.: Direct observation of frost wedging in alpine bedrock, *Earth Surf. Process. Landforms*, 26, 601–  
1082 614, <https://doi.org/10.1002/esp.208>, 2001.

1083 Matsuoka, N.: Frost weathering and rockwall erosion in the southeastern Swiss Alps: Long-term (1994–2006)  
1084 observations, *Geomorphology*, 99, 353–368, <https://doi.org/10.1016/j.geomorph.2007.11.013>, 2008.

1085 Messenzehl, K., Meyer, H., Otto, J.-C., Hoffmann, T., and Dikau, R.: Regional-scale controls on the spatial  
1086 activity of rockfalls (Turtmann Valley, Swiss Alps) — A multivariate modeling approach, *Geomorphology*, 287,  
1087 29–45, <https://doi.org/10.1016/j.geomorph.2016.01.008>, 2017.

1088 Murton, J. B., Peterson, R., and Ozouf, J.-C.: Bedrock Fracture by Ice Segregation in Cold Regions, *Science*, 314,  
1089 1127–1129, <https://doi.org/10.1126/science.1132127>, 2006.

1090 Mutz, S. G. and Ehlers, T. A.: Detection and explanation of spatiotemporal patterns in Late Cenozoic  
1091 palaeoclimate change relevant to Earth surface processes, *Earth Surf. Dynam.*, 7, 663–679,  
1092 <https://doi.org/10.5194/esurf-7-663-2019>, 2019.

1093 Mutz, S. G., Ehlers, T. A., Werner, M., Lohmann, G., Stepanek, C., and Li, J.: Estimates of late Cenozoic climate  
1094 change relevant to Earth surface processes in tectonically active orogens, *Earth Surf. Dynam.*, 6, 271–301,  
1095 <https://doi.org/10.5194/esurf-6-271-2018>, 2018.

1096 Otto-Bliesner, B. L., Brady, E. C., Clauzet, G., Tomas, R., Levis, S., and Kothavala, Z.: Last Glacial Maximum  
1097 and Holocene Climate in CCSM3, *J. Climate*, 19, 2526–2544, <https://doi.org/10.1175/JCLI3748.1>, 2006.

1098 Peizhen, Z., Molnar, P., and Downs, W. R.: Increased sedimentation rates and grain sizes 2±4 Myr ago due to the  
1099 influence of climate change on erosion rates, *410, 7*, 2001.

1100 Perron, J. T.: Climate and the Pace of Erosional Landscape Evolution, 45, 561–591,  
1101 <https://doi.org/10.1146/annurev-earth-060614-105405>, 2017.

1102 Pickett, E. J., Harrison, S. P., Hope, G., Harle, K., Dodson, J. R., Peter Kershaw, A., Colin Prentice, I., Backhouse,  
1103 J., Colhoun, E. A., D’Costa, D., Flenley, J., Grindrod, J., Haberle, S., Hassell, C., Kenyon, C., Macphail, M.,  
1104 Martin, H., Martin, A. H., McKenzie, M., Newsome, J. C., Penny, D., Powell, J., Ian Raine, J., Southern, W.,  
1105 Stevenson, J., Sutra, J.-P., Thomas, I., Kaars, S., and Ward, J.: Pollen-based reconstructions of biome distributions  
1106 for Australia, Southeast Asia and the Pacific (SEAPAC region) at 0, 6000 and 18,000 14C yr BP: Palaeovegetation  
1107 patterns for Australia and Southeast Asia, 31, 1381–1444, <https://doi.org/10.1111/j.1365-2699.2004.01001.x>,  
1108 2004.

1109 Prentice, I. C., Jolly, D., and BIOME 6000 Participants: Mid-Holocene and glacial-maximum vegetation  
1110 geography of the northern continents and Africa, *J Biogeography*, 27, 507–519, <https://doi.org/10.1046/j.1365-2699.2000.00425.x>, 2000.

1111



1112 Rangwala, I. and Miller, J. R.: Climate change in mountains: a review of elevation-dependent warming and its  
1113 possible causes, *Climatic Change*, 114, 527–547, <https://doi.org/10.1007/s10584-012-0419-3>, 2012.

1114 Raymo, M. E. and Ruddiman, W. F.: Tectonic forcing of late Cenozoic climate, *Nature*, 359, 117–122,  
1115 <https://doi.org/10.1038/359117a0>, 1992.

1116 Rempel, A. W., Marshall, J. A., and Roering, J. J.: Modeling relative frost weathering rates at geomorphic scales,  
1117 *Earth and Planetary Science Letters*, 453, 87–95, <https://doi.org/10.1016/j.epsl.2016.08.019>, 2016.

1118 Rode, M., Schnepfleitner, H., and Sass, O.: Simulation of moisture content in alpine rockwalls during freeze-thaw  
1119 events: Simulation of Moisture Content in Alpine Rock Walls, *Earth Surf. Process. Landforms*, 41, 1937–1950,  
1120 <https://doi.org/10.1002/esp.3961>, 2016.

1121 Roeckner, E., Bäuml, G., Bonaventura, L., Brokopf, R., Esch, M., Giorgetta, M., Hagemann, S., Kirchner, I.,  
1122 Kornblueh, L., Manzini, E., Rhodin, A., Schlese, U., Schulzweida, U., and Tompkins, A.: The atmospheric general  
1123 circulation model ECHAM 5. PART I: Model description, Max Planck Institute for Meteorology, Hamburg,  
1124 Germany, 2003.

1125 Sarnthein, M., Gersonde, R., Niebler, S., Pflaumann, U., Spielhagen, R., Thiede, J., Wefer, G., and Weinelt, M.:  
1126 Overview of Glacial Atlantic Ocean Mapping (GLAMAP 2000): GLAMAP 2000 OVERVIEW,  
1127 *Paleoceanography*, 18, n/a-n/a, <https://doi.org/10.1029/2002PA000769>, 2003.

1128 Savi, S., Delunel, R., and Schlunegger, F.: Efficiency of frost-cracking processes through space and time: An  
1129 example from the eastern Italian Alps, *Geomorphology*, 232, 248–260,  
1130 <https://doi.org/10.1016/j.geomorph.2015.01.009>, 2015.

1131 Schaller, M. and Ehlers, T. A.: Comparison of soil production, chemical weathering, and physical erosion rates  
1132 along a climate and ecological gradient (Chile) to global observations, *Earth Surf. Dynam.*, 10, 131–150,  
1133 <https://doi.org/10.5194/esurf-10-131-2022>, 2022.

1134 Schmid, M., Ehlers, T. A., Werner, C., Hickler, T., and Fuentes-Espoz, J.-P.: Effect of changing vegetation and  
1135 precipitation on denudation – Part 2: Predicted landscape response to transient climate and vegetation cover over  
1136 millennial to million-year timescales, 6, 859–881, <https://doi.org/10.5194/esurf-6-859-2018>, 2018.

1137 Simmons, A. J., Burridge, D. M., Jarraud, M., Girard, C., and Wergen, W.: The ECMWF medium-range prediction  
1138 models development of the numerical formulations and the impact of increased resolution, *Meteorol. Atmos. Phys.*,  
1139 40, 28–60, <https://doi.org/10.1007/BF01027467>, 1989.

1140 Sohl, L., Chandler, M., Schmunk, R., Mankoff, K., Jonas, J., Foley, K., and Dowsett, H.: PRISM3/GISS  
1141 Topographic Reconstruction, 2009.

1142 Sowers, T., Alley, R. B., and Jubenville, J.: Ice Core Records of Atmospheric N<sub>2</sub>O Covering the Last 106,000  
1143 Years, *Science*, 301, 945–948, <https://doi.org/10.1126/science.1085293>, 2003.

1144 Starke, J., Ehlers, T. A., and Schaller, M.: Latitudinal effect of vegetation on erosion rates identified along western  
1145 South America, *Science*, 367, 1358–1361, <https://doi.org/10.1126/science.aaz0840>, 2020.

1146 Stepanek, C. and Lohmann, G.: Modelling mid-Pliocene climate with COSMOS, *Geosci. Model Dev.*, 5, 1221–  
1147 1243, <https://doi.org/10.5194/gmd-5-1221-2012>, 2012.

1148 Turcotte, D. and Schubert, G.: *Geodynamics*, 3rd ed., Cambridge University Press,  
1149 <https://doi.org/10.1017/CBO9780511843877>, 2014.

1150 Valla, P. G., Shuster, D. L., and van der Beek, P. A.: Significant increase in relief of the European Alps during  
1151 mid-Pleistocene glaciations, *Nature Geosci.*, 4, 688–692, <https://doi.org/10.1038/ngeo1242>, 2011.

1152 Walder, J. S. and Hallet, B.: A theoretical model of the fracture of rock during freezing, *GSA Bulletin*, 96, 336–  
1153 346, [https://doi.org/10.1130/0016-7606\(1985\)96<336:ATMOTF>2.0.CO;2](https://doi.org/10.1130/0016-7606(1985)96<336:ATMOTF>2.0.CO;2), 1985.

1154 Wang, X., Schmidt, B., Otto, M., Ehlers, T. A., Mutz, S. G., Botsyun, S., and Scherer, D. . Sensitivity of water  
1155 balance in the Qaidam Basin to the mid-Pliocene climate. *Journal of Geophysical Research: Atmospheres*, 126,  
1156 e2020JD033965. <https://doi.org/10.1029/2020JD033965>, 2021

1157 Wei, W. and Lohmann, G.: Simulated Atlantic Multidecadal Oscillation during the Holocene, 25, 6989–7002,  
1158 <https://doi.org/10.1175/JCLI-D-11-00667.1>, 2012.

1159 Werner, C., Schmid, M., Ehlers, T. A., Fuentes-Espoz, J. P., Steinkamp, J., Forrest, M., Liakka, J., Maldonado,  
1160 A., and Hickler, T.: Effect of changing vegetation and precipitation on denudation – Part 1: Predicted vegetation  
1161 composition and cover over the last 21 thousand years along the Coastal Cordillera of Chile, 6, 829–858,  
1162 <https://doi.org/10.5194/esurf-6-829-2018>, 2018.

1163 Whipple, K. X.: The influence of climate on the tectonic evolution of mountain belts, *Nature Geoscience*, 2, 730–  
1164 730, <https://doi.org/10.1038/ngeo638>, 2009.

1165 Wieder, W.: RegridDED Harmonized World Soil Database v1.2, <https://doi.org/10.3334/ornlidaac/1247>, 2014.

1166

Page 13: [1] Deleted      Microsoft Office User      4/14/22 11:45:00 AM

Page 17: [2] Deleted      Microsoft Office User      4/15/22 10:50:00 AM

3.1.1. Page 20: [3] Deleted      Microsoft Office User      4/14/22 11:45:00 AM

## Supplementary material

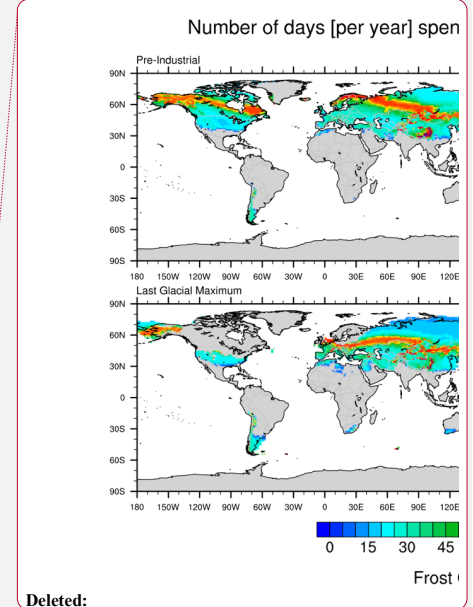
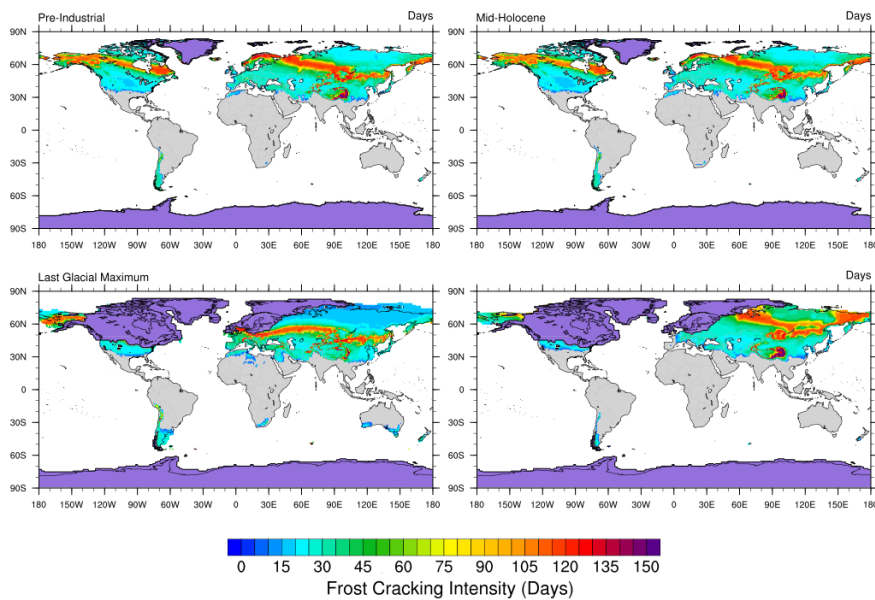
### 1. Model 1: FCI as a function of frost cracking window (FCW)

In Model 1, the FCI is calculated as a function of the number of days bedrock spent in frost cracking window (between  $-8^{\circ}\text{C}$  to  $-3^{\circ}\text{C}$ ), and ranges between 0 to 155 days a year for all the time slices considered (Fig. 6). The highest values are observed in mid to high-latitudes ( $30^{\circ}\text{N} - 60^{\circ}\text{N}$  and  $30^{\circ}\text{S} - 60^{\circ}\text{S}$ ) and coincide with ground surface MATs ranging between  $-10^{\circ}\text{C}$  and  $5^{\circ}\text{C}$ . This is the case in all time-slices as frost cracking intensity is highly dependent on MAT. In the Pliocene, the warmest of investigated climates, the maximum in FCI values are found Polar Regions.

A prominent band of frost cracking is observed for the PI and MH simulations (yellow regions, Fig. 6) on the North American and Eurasian continents in the latitudinal range of  $35^{\circ}\text{N} - 80^{\circ}\text{N}$  and  $30^{\circ}\text{N} - 80^{\circ}\text{N}$  respectively. Here, the FCI values are  $\sim 120 - 130$  days between  $50^{\circ}\text{N}$  and  $70^{\circ}\text{N}$  for the North America and  $45^{\circ}\text{N}$  and  $70^{\circ}\text{N}$  for Eurasia. Regions to the north or south of this band of high FCI values have lower values because the temperatures are cooler or warmer, respectively, than the frost cracking window. The highest FCI values occur in eastern margin of the Tibetan Plateau ( $\sim 150$  days). For South America, low values of FCI are observed in the Andes Mountains and range from 0 to 25 days between  $15^{\circ}\text{S}$  and  $50^{\circ}\text{S}$ . Also, small values (15 – 30 days) are observed on the periphery of Antarctica.

In the LGM, there were ice sheets for most of North America and Europe. The highest FCI values ( $\sim 105$  days) can be observed in the mid- to high latitudes of North Eurasia ( $40^{\circ}\text{N} - 60^{\circ}\text{N}$ ). For South America, frost cracking is observed between  $15^{\circ}\text{S}$  and  $50^{\circ}\text{S}$  with lower values of FCI in the north ( $\sim 25 - 65$  days).

In the Pliocene, North America ( $55^{\circ}\text{N} - 80^{\circ}\text{N}$ ) and Eurasia ( $45^{\circ}\text{N} - 80^{\circ}\text{N}$ ) contain high FCI values of up to  $\sim 120$  days, with the highest values located again on the eastern margin of the Tibetan Plateau ( $\sim 155$  days). In contrast to other time-slices, high FCI values are observed in southern Greenland ( $\sim 130$  days), and lower values in the north ( $\sim 30 - 50$  days) due to the cooler temperatures there (more often below the frost cracking window). In South America, lower values ( $\sim 10 - 30$  days) are predicted in the LGM, and higher values along the western periphery of Antarctica.



Deleted:

**Figure S.1. Predicted days in the FCI (Model 1) determined by the number of days spent in frost cracking window ( $-8\text{ }^{\circ}\text{C}$  -  $-3\text{ }^{\circ}\text{C}$ ) for Pre-Industrial (top-left), Mid-Holocene (top-right), Last Glacial Maximum (bottom-left), and Pliocene (bottom-right) times (unit:  $^{\circ}\text{C m}$ ). The grey areas in plots indicates the absence of frost cracking. For all time slices, the regions covered by ice were removed from the calculation and are highlighted in violet color (Bracannot et al., 2012). For the PLIO results, the LGM ice cover is used, since the assumption of modern soil depth is heavily violated in these regions.**

## 2. Model 2: FCI as a function of thermal gradient

The FCI observed in Model 2 is in the range of  $0 - 1400\text{ }^{\circ}\text{C}$  from  $30\text{ }^{\circ}\text{N} - 80\text{ }^{\circ}\text{N}$  and  $20\text{ }^{\circ}\text{S} - 80\text{ }^{\circ}\text{S}$  for all time-slices (Fig. 7). Similar to Model 1, in Model 2 the maximum values are observed as band of high values across the mid to high latitudes ( $30\text{ }^{\circ}\text{N} - 60\text{ }^{\circ}\text{N}$  and  $30\text{ }^{\circ}\text{S} - 60\text{ }^{\circ}\text{S}$ ), coinciding with MAT values in the range of ( $-10\text{ }^{\circ}\text{C} - 5\text{ }^{\circ}\text{C}$ ). These areas cover much of northern Asia. The highest values are observed in western Russia and Northern China ( $850\text{ }^{\circ}\text{C} - 1050\text{ }^{\circ}\text{C}$ ).

In the PI and MH simulations, the regions marked by high potential for frost cracking (with FCI up to  $\sim 900\text{ }^{\circ}\text{C}$ ) include North America ( $40\text{ }^{\circ}\text{N} - 60\text{ }^{\circ}\text{N}$ ) and Eurasia ( $30\text{ }^{\circ}\text{N} - 60\text{ }^{\circ}\text{N}$ ). FCI values in the Andes Mountains in South America ( $15\text{ }^{\circ}\text{S} - 50\text{ }^{\circ}\text{S}$ ) and western periphery of Antarctica ( $180\text{ }^{\circ}\text{W} - 0\text{ }^{\circ}\text{W}$ ) range between  $\sim 150\text{ }^{\circ}\text{C}$  and  $400\text{ }^{\circ}\text{C}$ . Also, the periphery of Greenland exhibits FCI values of  $\sim 200\text{ }^{\circ}\text{C}$ .

In the LGM simulation, the highest FCI values are observed in North America ( $35\text{ }^{\circ}\text{N} - 45\text{ }^{\circ}\text{N}$ ) and Eurasia ( $35\text{ }^{\circ}\text{N} - 55\text{ }^{\circ}\text{N}$ ) with the values ranging between  $\sim 400\text{ }^{\circ}\text{C} - 900\text{ }^{\circ}\text{C}$ . Also, high FCI values are observed for South America ( $15\text{ }^{\circ}\text{S} - 55\text{ }^{\circ}\text{S}$ ) and New Zealand and range between  $\sim 100\text{ }^{\circ}\text{C}$  and  $800\text{ }^{\circ}\text{C}$ . Low values of FCI ( $\sim 0 - 200\text{ }^{\circ}\text{C}$ ) are observed in the northern and southern Africa and Australia.

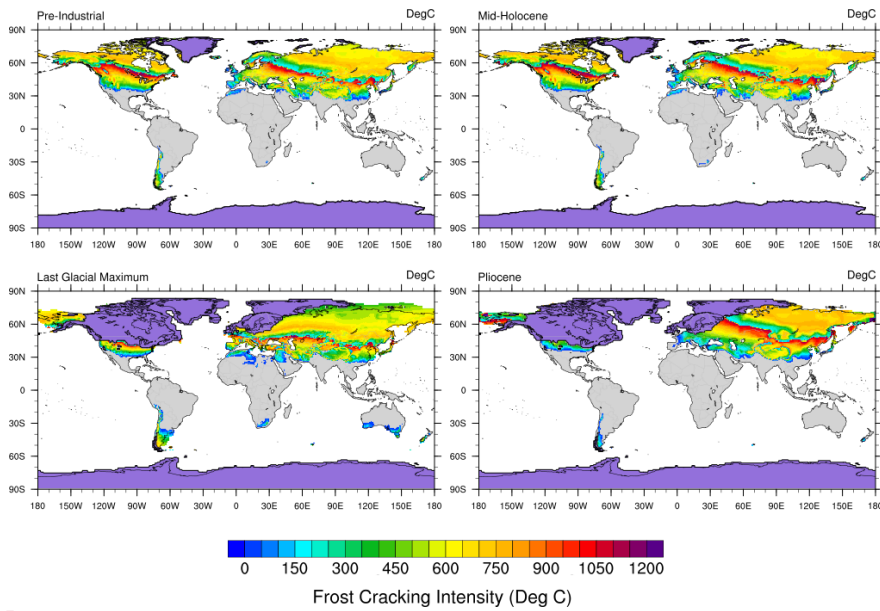
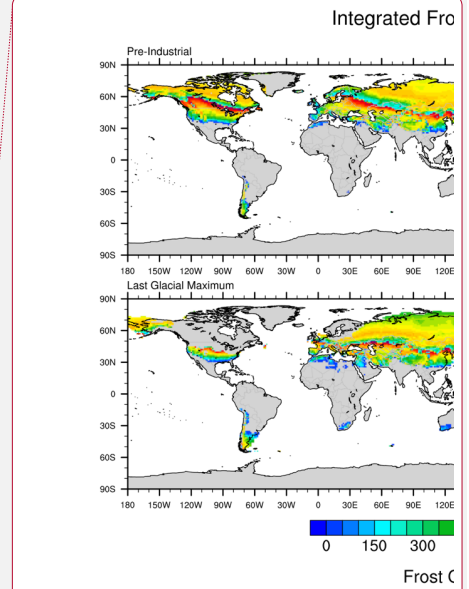


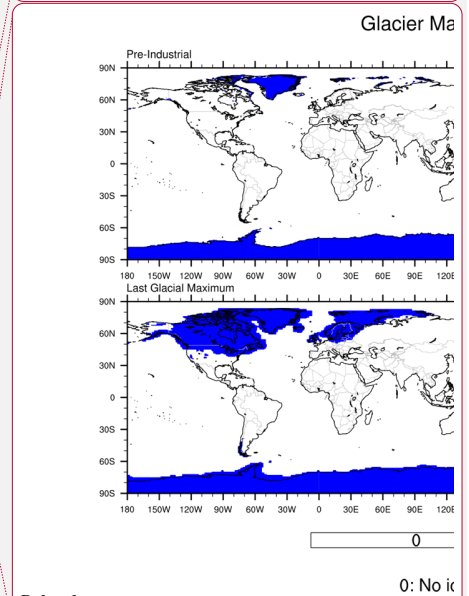
Figure S.2. Model 2 output with Integrated FCI as a function of thermal gradient of the bedrock for Pre-Industrial (top-left), Mid-Holocene (top-right), Last Glacial Maximum (bottom-left), and Pliocene (bottom-right) times (unit: °C). The grey areas in plots indicates the absence of frost cracking. For all time slices, the regions covered by ice were removed from the calculation and are highlighted in violet color (Bracannot et al., 2012). For the PLIO results, the LGM ice cover is used, since the assumption of modern soil depth is heavily violated in these regions.

For the Pliocene, similar to Model 1, the highest FCI values are observed in higher latitudes in North America and Eurasia (~950 °C), and Greenland shows high values of ~ 200 °C – 650 °C. Low FCI values are observed in South America and the periphery of Antarctica (~ 0 °C – 200 °C).



Deleted:

Deleted: .



Deleted:

Deleted: Figure S.3. Glacier Mask for Pre-Industrial (top-left), Mid-Holocene (top-right), Last Glacial Maximum (bottom-left), and Pliocene (bottom-right) times (unit: fraction). NOTE: FCI data from Model 3 is attached at netCDF format in a single file (Integrated\_FCI.nc) with different time slices (description is provided in the file itself).